MNRAS **000**, 1–28 (2019) Preprint 4 November 2021 Compiled using MNRAS LATEX style file v3.0

Trend Filtering: A Modern Statistical Tool for Time-Domain Astronomy and Astronomical Spectroscopy

Collin A. Politsch,[1,2,3]★ Jessi Cisewski-Kehe,[4] Rupert A. C. Croft,[3,5,6] and Larry Wasserman[1,2,3]

[1] *Department of Statistics & Data Science, Carnegie Mellon University, Pittsburgh, PA 15213*
[2] *Machine Learning Department, Carnegie Mellon University, Pittsburgh, PA 15213*
[3] *McWilliams Center for Cosmology, Carnegie Mellon University, Pittsburgh, PA 15213*
[4] *Department of Statistics and Data Science, Yale University, New Haven, CT 06520*
[5] *Department of Physics, Carnegie Mellon University, Pittsburgh, PA 15213*
[6] *School of Physics, University of Melbourne, VIC 3010, Australia*

arXiv:1908.07151v2 [astro-ph.IM] 16 Dec 2019

Accepted XXX. Received YYY; in original form 2019 August 20

ABSTRACT

The problem of denoising a one-dimensional signal possessing varying degrees of smoothness is ubiquitous in time-domain astronomy and astronomical spectroscopy. For example, in the time domain, an astronomical object may exhibit a smoothly varying intensity that is occasionally interrupted by abrupt dips or spikes. Likewise, in the spectroscopic setting, a noiseless spectrum typically contains intervals of relative smoothness mixed with localized higher frequency components such as emission peaks and absorption lines. In this work, we present trend filtering, a modern nonparametric statistical tool that yields significant improvements in this broad problem space of denoising *spatially heterogeneous* signals. When the underlying signal is spatially heterogeneous, trend filtering is superior to any statistical estimator that is a linear combination of the observed data—including kernels, LOESS, smoothing splines, Gaussian process regression, and many other popular methods. In the spirit of illustrating the broad utility of trend filtering, we discuss its relevance to a diverse set of spectroscopic and time-domain studies. The observations we discuss are (1) the Lyman-α forest of quasar spectra; (2) more general spectroscopy of quasars, galaxies, and stars; (3) stellar light curves with transiting exoplanet(s); (4) eclipsing binary light curves; and (5) supernova light curves. We study the Lyman-α forest in the greatest detail—using trend filtering to map the large-scale structure of the intergalactic medium along quasar-observer sightlines. The remaining studies broadly center around the themes of using trend filtering to estimate observable parameters and generate spectral/light-curve templates.

Key words: Methods: statistical, techniques: spectroscopic, cosmology: observations, stars: planetary systems, stars: binaries: eclipsing, supernovae: general

1 INTRODUCTION

Many astronomical observations produce one-dimensional data with unknown or varying degrees of smoothness. These include data from time-domain astronomy, where transient events such as supernovae can show light-curve variations on timescales ranging from seconds to years (e.g., Dimitriadis et al. 2017; Tolstov et al. 2019). Similarly, in astronomical spectroscopy, with wavelength (or frequency) as the independent variable, sharp absorption or emission-line features can be present alongside smoothly varying black-body or other continuum radiation (see, e.g., Tennyson 2019). In each of these general settings, we observe a signal plus noise and would like to denoise the signal as accurately as possible. Indeed the set of statistical tools available for addressing this general problem is quite vast. Commonly used nonparametric regression methods include kernel smoothers (e.g., Hall et al. 2002; Croft et al. 2002), local polynomial regression (LOESS; e.g., Maron & Howes 2003; Persson et al. 2004), splines (e.g., Peiris & Verde 2010;

★ E-mail: capolitsch@cmu.edu

© 2019 The Authors

Contreras et al. 2010; Dhawan et al. 2015), Gaussian process regression (e.g., Gibson et al. 2012; Aigrain et al. 2016; Gómez-Valent & Amendola 2018), and wavelet decompositions (e.g., Fligge & Solanki 1997; Theuns & Zaroubi 2000; Golkhou & Butler 2014). A rich and elegant statistical literature exists on the theoretical and practical achievements of these methods (see, e.g., Györfi et al. 2002; Wasserman 2006; Hastie et al. 2009 for general references). However, when the underlying signal is *spatially heterogeneous*, i.e. exhibits varying degrees of smoothness, the power of classical statistical literature is quite limited. Kernels, LOESS, smoothing splines, and Gaussian process regression belong to a broad family of nonparametric methods called *linear smoothers*, which has been shown to be uniformly suboptimal for estimating spatially heterogeneous signals (Nemirovskii et al. 1985; Nemirovskii 1985; Donoho & Johnstone 1998). The common limitation of these methods is that they are not locally adaptive; i.e., by construction, they do not adapt to local degrees of smoothness in a signal. In particular, continuing with the example of a smoothly varying signal with occasional sharp features, a linear smoother will tend to oversmooth the sharp features and/or overfit the smooth regions in its effort to optimally balance statistical bias and variance. Considerable effort has been made to address this problem by locally varying the hyperparameter(s) of a linear smoother. For example, locally varying the kernel bandwidth (e.g., Muller & Stadtmuller 1987; Fan & Gijbels 1992, 1995; Lepski et al. 1997; Gijbels & Mammen 1998) irregularly varying spline knot locations (e.g., De Boor 1974; Jupp 1978; Dimatteo et al. 2001), and constructing non-stationary covariance functions for Gaussian process regression (e.g., Schmidt & O'Hagan 2003; Paciorek & Schervish 2004, 2006). However, since hyperparameters typically need to be estimated from the data, such exponential increases in the hyperparameter complexity severely limit the practicality of choosing the hyperparameters in a fully data-driven, generalizable, and computationally efficient fashion. Wavelet decompositions offer an elegant solution to the problem of estimating spatially heterogeneous signals, providing both statistical optimality (e.g., Donoho & Johnstone 1994, 1998) and only requiring data-driven tuning of a single (scalar) hyperparameter. Wavelets, however, possess the practical limitation of requiring a stringent analysis setting, e.g. equally-spaced inputs and sample size equal to a power of two, among other provisions; and when these conditions are violated, the optimality guarantees are void. So, seemingly at an impasse, the motivating question for this work is *can we have the best of both worlds?* More precisely, is there a statistical tool that simultaneously possesses the following properties:

- **P1.** Statistical optimality for estimating spatially heterogeneous signals
- **P2.** Practical analysis assumptions; for example, not limited to equally-spaced inputs
- **P3.** Practical computational speed
- **P4.** A one-dimensional hyperparameter space, with automatic data-driven methods for selection

In this paper we introduce trend filtering (Steidl et al. 2006; Kim et al. 2009; Tibshirani 2014), a statistical method that is new to the astronomical literature and provides a strong affirmative answer to this question.

The layout of the paper is as follows. In Section 2 we provide both theoretical and empirical evidence of the superiority of trend filtering for estimating spatially heterogeneous signals compared to classical statistical methods. In Section 3 we introduce trend filtering, including a general overview of the estimator's machinery, its connection to spline methods, automatic methods for choosing the hyperparameter, uncertainty quantification, generalizations, and recommended software implementations in various programming languages. In Section 4 we use trend filtering to rigorously study the Lyman-α forest of quasar spectra—a series of absorption features that can be used as a tracer of the matter density distribution along quasar-observer lines of sight. Finally, in Section 5 we illustrate the utility of trend filtering to a much wider variety of one-dimensional problems across astronomical spectroscopy and time-domain astronomy (necessarily discussing each application less comprehensively than our Lyman-α forest study). In particular, we discuss how trend filtering can be used to (1) generate galaxy, quasar, and stellar spectral templates and produce robust estimates of emission-line parameters; (2) model exoplanet transit events in phase-folded stellar light curves, providing transit depth and duration measurements; (3) improve upon the `polyfit` algorithm of Prša et al. (2008) for denoising phase-folded eclipsing binary light curves; (4) generate supernova light-curve templates and produce nonparametric estimates of the observable parameters—e.g., the maximum apparent magnitude, the time of maximum, and the decline rate. Beyond its uses for astronomical data analysis, we also briefly discuss its relevance to large-scale one-dimensional data reduction and compression.

2 CLASSICAL STATISTICAL METHODS AND THEIR LIMITATIONS

We begin this section by providing background and motivation for the nonparametric approach to estimating (or denoising) signals. We then discuss statistical optimality for estimating spatially heterogeneous signals, with an emphasis on providing evidence for the claim that trend filtering is broadly superior to classical statistical methods in this setting. Finally, we end this section by illustrating this superiority with a direct empirical comparison of trend filtering and several popular classical methods on simulated observations of a spatially heterogeneous signal.

2.1 Nonparametric regression

Suppose we observe noisy measurements of a response variable of interest (e.g., flux, magnitude, photon counts) according to the data generating process (DGP)

$$f(t_i) = f_0(t_i) + \epsilon_i, \qquad i = 1, \ldots, n \quad (1)$$

where $f_0(t_i)$ is the signal at input t_i (e.g., a time or wavelength) and ϵ_i is the noise at t_i that contaminates the signal, giving rise to the observation $f(t_i)$. Let $t_1, \ldots, t_n \in (a, b)$ denote the observed input interval and $\mathbb{E}[\epsilon_i] = 0$ (where we use $\mathbb{E}[\cdot]$ to denote mathematical expectation). Here, the general statistical problem is to estimate (or denoise) the underlying signal f_0 from the observations as accurately as possible. In the nonparametric setting, we refrain from making strong

a priori assumptions about f_0 that could lead to significant modeling bias, e.g. assuming a power law or a light-curve/spectral template fit. Mathematically, a nonparametric approach is defined through the deliberately weak assumption $f_0 \in \mathcal{F}$ (i.e. the signal belongs to the function class $\mathcal{F}$) where $\mathcal{F}$ is *infinite-dimensional*. In other words, the assumed class of all possible signals $\mathcal{F}$ cannot be spanned by a finite number of parameters. Contrast this to the assumption that the signal follows a pth degree power law, i.e. $f_0 \in \mathcal{F}_{\mathrm{PL}}$ where

$$\mathcal{F}_{\mathrm{PL}} = \left\{ f_0 : f_0(t) = \beta_0 + \sum_{j=1}^{p} \beta_j t^j \right\}, \tag{2}$$

a class that is spanned by $p+1$ parameters. Similarly, given a set of p spectral/light-curve templates $b_1(t), \ldots, b_p(t)$, the usual template-fitting assumption is that $f_0 \in \mathcal{F}_{\mathrm{TEMP}}$ where

$$\mathcal{F}_{\mathrm{TEMP}} = \left\{ f_0 : f_0(t) = \beta_0 + \sum_{j=1}^{p} \beta_j b_j((t-s)/v) \right\} \tag{3}$$

and s and v are horizontal shift and stretch hyperparameters, respectively. Both (2) and (3) represent very stringent assumptions about the underlying signal f_0. If the signal is anything other than exactly a power law in t—a highly unlikely occurrence—nontrivial statistical bias will arise by modeling it as such. Likewise, if a class of signals has a rich physical diversity (e.g., Type Ia supernova light curves; Woosley et al. 2007) that is not sufficiently spanned by the library of templates used in modeling, then statistical biases will arise. Depending on the size of the imbalance between class diversity and the completeness of the template basis, the biases could be significant. Moreover, these biases are rarely tracked by uncertainty quantification. To be clear, this is not a uniform criticism of template-fitting. For example, templates are exceptionally powerful tools for object classification and redshift estimation (e.g., Howell et al. 2005, Bolton et al. 2012). Furthermore, much of our discussion in Section 5 centers around utilizing the flexible nonparametric nature of trend filtering to construct more complete spectral/light-curve template libraries for various observational objects and transient events.

Let $\widehat{f_0}$ be any statistical estimator for the signal f_0, derived from the noisy observations in (1). Further, let $p_t(t)$ denote the probability density function (pdf) that specifies the sampling distribution of the inputs on the interval (a, b), and let $\sigma^2(t) = \mathrm{Var}(\epsilon(t))$ denote the noise level at input t. In order to assess the accuracy of the estimator it is common to consider the mean-squared prediction error (MSPE):

$$R(\widehat{f_0}) = \mathbb{E}\big[(\widehat{f_0} - f)^2\big] \tag{4}$$

$$= \mathbb{E}\big[(\widehat{f_0} - f_0)^2\big] + \overline{\sigma}^2 \tag{5}$$

$$= \int_a^b \Big(\mathrm{Bias}^2(\widehat{f_0}(t)) + \mathrm{Var}(\widehat{f_0}(t))\Big) \cdot p_t(t)dt + \overline{\sigma}^2, \tag{6}$$

where

$$\mathrm{Bias}(\widehat{f_0}(t)) = \mathbb{E}[\widehat{f_0}(t)] - f_0(t) \tag{7}$$

$$\mathrm{Var}(\widehat{f_0}(t)) = \mathbb{E}\Big(\widehat{f_0}(t) - \mathbb{E}[\widehat{f_0}(t)]\Big)^2 \tag{8}$$

$$\overline{\sigma}^2 = \int_a^b \sigma^2(t) \cdot p_t(t)dt. \tag{9}$$

The equality in (6) is commonly referred to as the bias-variance decomposition. The first term is the squared bias of the estimator $\widehat{f_0}$ (integrated over the input interval) and intuitively measures how appropriate the chosen statistical estimator is for modeling the observed phenomenon. The second term is the variance of the estimator that measures how stable or sensitive the estimator is to the observed data. And the third term is the irreducible error—the minimum prediction error we cannot hope to improve upon. The bias-variance decomposition therefore illustrates that an optimal estimator is one that combines appropriate modeling assumptions (low bias) with high stability (low variance).

2.1.1 *Statistical optimality (minimax theory)*

In this section, we briefly discuss a mathematical framework for evaluating the performance of statistical methods over nonparametric signal classes in order to demonstrate that the superiority of trend filtering is a highly general result. Ignoring the irreducible error, the problem of minimizing the MSPE of a statistical estimator can be equivalently stated as a minimization of the first term in (5)—the mean-squared estimation error (MSEE). In practice, low bias is attained by only making very weak assumptions about what the underlying signal may look like, e.g. f_0 has k continuous derivatives. An ideal statistical estimator for estimating signals in such a class (call it $\mathcal{F}$) may then be defined as

$$\inf_{\widehat{f_0}} \Big(\sup_{f_0 \in \mathcal{F}} \mathbb{E}\big[(\widehat{f_0} - f_0)^2\big] \Big). \tag{10}$$

That is, we would like our statistical estimator to be the minimizer (infimum) of the worst-case (supremum) MSEE over the signal class $\mathcal{F}$. This is rarely a mathematically tractable problem for any practical signal class $\mathcal{F}$. A more tractable approach is to consider how the worst-case MSEE behaves as a function of the sample size n. A reasonable baseline metric for a statistical estimator is to require that it satisfies

$$\sup_{f_0 \in \mathcal{F}} \mathbb{E}\big[(\widehat{f_0} - f_0)^2\big] \to 0 \tag{11}$$

as $n \to \infty$. That is, for any signal $f_0 \in \mathcal{F}$, when a large amount of data is available, $\widehat{f_0}$ gets arbitrarily close to the true signal. In any practical situation, this is not true for parametric models because the bias component of the bias-variance decomposition never vanishes. This, however, is a widely-held—perhaps, defining—property of nonparametric methods. Therefore, in order to distinguish optimality among nonparametric estimators, we require a stronger metric. In particular, we study *how quickly* the worst-case error goes to zero as more data is observed. This is the core idea of a rich area of statistical literature called *minimax theory* (see, e.g., Van der Vaart 1998; Wasserman 2006; Tsybakov 2008). For many infinite-dimensional classes of signals, theoretical lower-bounds exist on the rate at which the MSEE of *any* statistical estimator can approach zero. Therefore, if a statistical estimator is shown to achieve that rate, it can be considered optimal for estimating that class of signals. Formally, letting $g(n)$ be the rate at which the MSEE of the theoretically optimal estimator (10) goes to zero (a monotonically decreasing function in n), we would like our

estimator $\widehat{f_0}$ to satisfy

$$\sup_{f_0 \in \mathcal{F}} \mathbb{E}\left[(\widehat{f_0} - f_0)^2\right] = O(g(n)), \tag{12}$$

where we use $O(\cdot)$ to denote big O notation. If this is shown to be true, we say the estimator *achieves the minimax rate over the signal class* $\mathcal{F}$. Loosely speaking, we are stating that a *minimax optimal* estimator is an estimator that learns the signal from the data just as quickly as the theoretical gold standard estimator (10).

2.1.2 Spatially heterogeneous signals

Thus far we have only specified that the signal underlying most one-dimensional astronomical observations should be assumed to belong to a class $\mathcal{F}$ that is infinite-dimensional (i.e. nonparametric). Further, in Section 2.1.1 we introduced the standard metric used to measure the performance of a statistical estimator over an infinite-dimensional class of signals. Recalling the discussion in the abstract and Section 1, trend filtering provides significant advances for estimating signals that exhibit varying degrees of smoothness across the input domain. We restate this definition below.

Definition. A *spatially heterogeneous* signal is a signal that exhibits varying degrees of smoothness in different regions of its input domain.

Example. A smooth light curve with abrupt transient events.

Example. An electromagnetic spectrum with smooth continuum radiation and sharp absorption/emission-line features.

To complement the above definition we may also loosely define a *spatially homogeneous signal* as a signal that is *either* smooth *or* wiggly[1] across its input domain, but not both. As "smoothness" can be quantified in various ways these definitions are intentionally mathematically imprecise. A class that is commonly considered in the statistical literature is the L_2 Sobolev class:

$$\mathcal{F}_{2,k}(C_1) := \left\{ f_0 : \int_a^b f_0^{(k)}(t)^2 dt < C_1 \right\}, \qquad C_1 > 0,\ k \in \mathbb{N}. \tag{13}$$

That is, an L_2 Sobolev class is a class of all signals such that the integral of the square (the "L_2 norm") of the kth derivative of each signal is less than some constant C_1. Statistical optimality in the sense of Section 2.1.1 for estimating signals in these classes (and some other closely related ones) is widely held among statistical methods in the classical toolkit; for example, kernel smoothers (Ibragimov & Hasminiskii 1980; Stone 1982), LOESS (Fan 1993; Fan et al. 1997), and smoothing splines (Nussbaum 1985). However, a seminal result by Nemirovskii et al. (1985) and Nemirovskii (1985) showed that a statistical estimator can be minimax optimal over signal classes of the form (13) and still perform quite poorly on other signals. In particular, the authors showed that, when considering the broader L_1 Sobolev class

$$\mathcal{F}_{1,k}(C_2) := \left\{ f_0 : \int_a^b \left| f_0^{(k)}(t) \right| dt < C_2 \right\}, \qquad C_2 > 0,\ k \in \mathbb{N}, \tag{14}$$

all linear smoothers[2]—including kernels, LOESS, smoothing splines, Gaussian process regression, and many other methods—are strictly suboptimal. The key difference between these two types of classes is that L_2 Sobolev classes are rich in spatially homogeneous signals but not spatially heterogeneous signals, while L_1 Sobolev classes[3] are rich in both (see, e.g., Donoho & Johnstone 1998).

The intuition of this result is that linear smoothers cannot optimally recover signals that exhibit varying degrees of smoothness across their input domain because they operate as if the signal possesses a fixed degree of smoothness. For example, this intuition is perhaps most clear when considering a kernel smoother with a fixed bandwidth. The result of Nemirovskii et al. (1985) and Nemirovskii (1985) therefore implies that, in order to achieve statistical optimality for estimating spatially heterogeneous signals, a statistical estimator must be nonlinear (more specifically, it must be locally adaptive). Tibshirani (2014) showed that trend filtering is minimax optimal for estimating signals in L_1 Sobolev classes. Since L_2 Sobolev classes are contained within L_1 Sobolev classes, this result also guarantees that trend filtering is also minimax optimal for estimating signals in L_2 Sobolev classes. Wavelets share this property, but require restrictive assumptions on the sampling of the data (Donoho & Johnstone 1994).

How large is this performance gap? The collective results of Nemirovskii et al. (1985), Nemirovskii (1985), and Tibshirani (2014) reveal that the performance gap between trend filtering and linear smoothers when estimating spatially heterogeneous signals is significant. For example, when $k = 0$, the minimax rate over L_1 Sobolev classes (which trend filtering achieves) is $n^{-2/3}$, but linear smoothers cannot achieve better than $n^{-1/2}$. To put this in perspective, this result says that the trend filtering estimator, training on n data points, learns these signals with varying smoothness as quickly as a linear smoother training on $n^{4/3}$ data points. As we demonstrate in the next section, this gap in theoretical optimality has clear practical consequences.

In order to minimize the pervasion of technical statistical jargon throughout the paper, henceforth we simply refer to a statistical estimator that achieves the minimax rate over L_2 Sobolev classes as *statistically optimal for estimating spatially homogeneous signals*, and we refer to a statistical estimator that achieves the minimax rate over L_1 Sobolev classes as *statistically optimal for estimating spatially heterogeneous signals*. As previously mentioned, the latter implies the former, but not vice versa.

[1] This is, in fact, a technical term used in the statistical literature.

[2] A *linear smoother* is a statistical estimator that is a linear combination of the observed data. Many popular statistical estimators, although often motivated from seemingly disparate premises, can be shown to fall under this definition. See, e.g., Wasserman (2006) for more details.

[3] The L_1 Sobolev class is often generalized to a nearly equivalent but slightly larger class—namely, signals with derivatives of bounded total variation. See Tibshirani (2014) for the generalized definition.

2.2 Empirical comparison

In this section we analyze noisy observations of a simulated spatially heterogeneous signal in order to compare the empirical performance of trend filtering and several classical statistical methods—namely, LOESS, smoothing splines, and Gaussian process regression. The mock observations are simulated on an unequally-spaced grid $t_1, \dots, t_n \sim \text{Unif}(0, 1)$ according to the data generating process

$$f(t_i) = f_0(t_i) + \epsilon_i \tag{15}$$

with

$$f_0(t_i) = 6 \sum_{k=1}^{3} (t_i - 0.5)^k + 2.5 \sum_{j=1}^{4} (-1)^j \phi_j(t_i), \tag{16}$$

where $\phi_j(t)$, $j = 1, \dots, 4$ are compactly-supported radial basis functions distributed throughout the input space and $\epsilon_i \sim N(0, 0.125^2)$. We therefore construct the signal f_0 to have a smoothly varying global trend with four sharp localized features—two dips and two spikes. The signal and noisy observations are shown in the top panel of Figure 1.

In order to facilitate the comparison of methods we utilize a metric for the total statistical complexity (i.e. total wiggliness) of an estimator known as the *effective degrees of freedom* (see, e.g., Tibshirani 2015). Formally, the effective degrees of freedom of an estimator $\widehat{f_0}$ is defined as

$$\text{df}(\widehat{f_0}) = \overline{\sigma}^{-2} \sum_{i=1}^{n} \text{Cov}(\widehat{f_0}(t_i), f(t_i)) \tag{17}$$

where $\overline{\sigma}^2$ is defined in (9). In Figure 1 we fix all estimators to have 55 effective degrees of freedom. This exercise provides insight into how each estimator relatively distributes its complexity across the input domain. In the second panel we see that the trend filtering estimate has sufficiently recovered the underlying signal, including both the smoothness of the global trend and the abruptness of the localized features. All three of the linear smoothers, on the other hand, severely oversmooth the localized peaks and dips. Gaussian process regression also exhibits some undesirable oscillatory features that do not correspond to any real trend in the signal. In order to better recover the localized features the linear smoothers require a more complex fit, i.e. smaller LOESS kernel bandwidth, smaller smoothing spline penalization, and smaller Gaussian process noise-signal variance. In Figure 2 we show the same comparison, but we grant the linear smoothers more complexity. Specifically, in order to recover the sharp features comparably with the trend filtering estimator with 55 effective degrees of freedom, the linear smoothers require 192 effective degrees of freedom—approximately 3.5 times the complexity. As a result, although they now adequately recover the peaks and dips, each linear smoother severely overfits the data in the other regions of the input domain, resulting in many spurious fluctuations.

As discussed in Section 2.1.2, the suboptimality of LOESS, smoothing splines, and Gaussian process regression illustrated in this example is an inherent limitation of the broad *linear smoother* family of statistical estimators. Linear smoothers are adequate tools for estimating signals that exhibit approximately the same degree of smoothness throughout their input domain. For example, in Section 4.3 we use LOESS to nonparametrically reconstruct the smooth background continuum radiation in quasar spectra. However, when a signal is expected to exhibit varying degrees of smoothness across its domain, a locally-adaptive statistical estimator is needed.

3 TREND FILTERING

Trend filtering, in its original form, was independently proposed in the computer vision literature (Steidl et al. 2006) and the applied mathematics literature (Kim et al. 2009), and has recently been further developed in the statistical and machine learning literature, most notably with Tibshirani & Taylor (2011), Tibshirani (2014), Wang et al. (2016), and Ramdas & Tibshirani (2016). This work is in no way related to the work of Kovács et al. (2005), which goes by a similar name. At a high level, trend filtering is closely related to two familiar nonparametric regression methods: variable-knot regression splines and smoothing splines. We elaborate on these relationships below.

3.1 Closely-related methods

Splines have long played a central role in estimating complex signals (see, e.g., De Boor 1978 and Wahba 1990 for general references). Formally, a kth order spline is a piecewise polynomial (i.e. piecewise power law) of degree k that is continuous and has $k-1$ continuous derivatives at the knots. As their names suggest, variable-knot regression splines and smoothing splines center around fitting splines to observational data. Recall from (1) the observational data generating process (DGP)

$$f(t_i) = f_0(t_i) + \epsilon_i, \qquad t_1, \dots, t_n \in (a, b), \tag{18}$$

where $f(t_i)$ is a noisy measurement of the signal $f_0(t_i)$, and $\mathbb{E}[\epsilon_i] = 0$. Given a set of knots $\kappa_1, \dots, \kappa_p \in (a, b)$, the space of all kth order splines on the interval (a, b) with knots at $\kappa_1, \dots, \kappa_p$ can be parametrized via a basis representation

$$m(t) = \sum_j \beta_j \eta_j(t), \tag{19}$$

where $\{\eta_j\}$ is typically the truncated power basis or B-spline basis. A suitable estimator for the signal f_0 may then be

$$\widehat{f_0}(t) = \sum_j \widehat{\beta}_j \eta_j(t), \tag{20}$$

where the $\widehat{\beta}_j$ are the ordinary least-squares (OLS) estimates of the basis coefficients. This is called a *regression spline*. The question of course remains where to place the knots.

3.1.1 *Variable-knot regression splines*

The variable-knot (or free-knot) regression spline approach is to consider all regression spline estimators with knots at a subset of the observed inputs, i.e. $\{\kappa_1, \dots, \kappa_p\} \subset \{t_1, \dots, t_n\}$ for all possible p. Formally, the variable-knot regression spline estimator is the solution to the following constrained

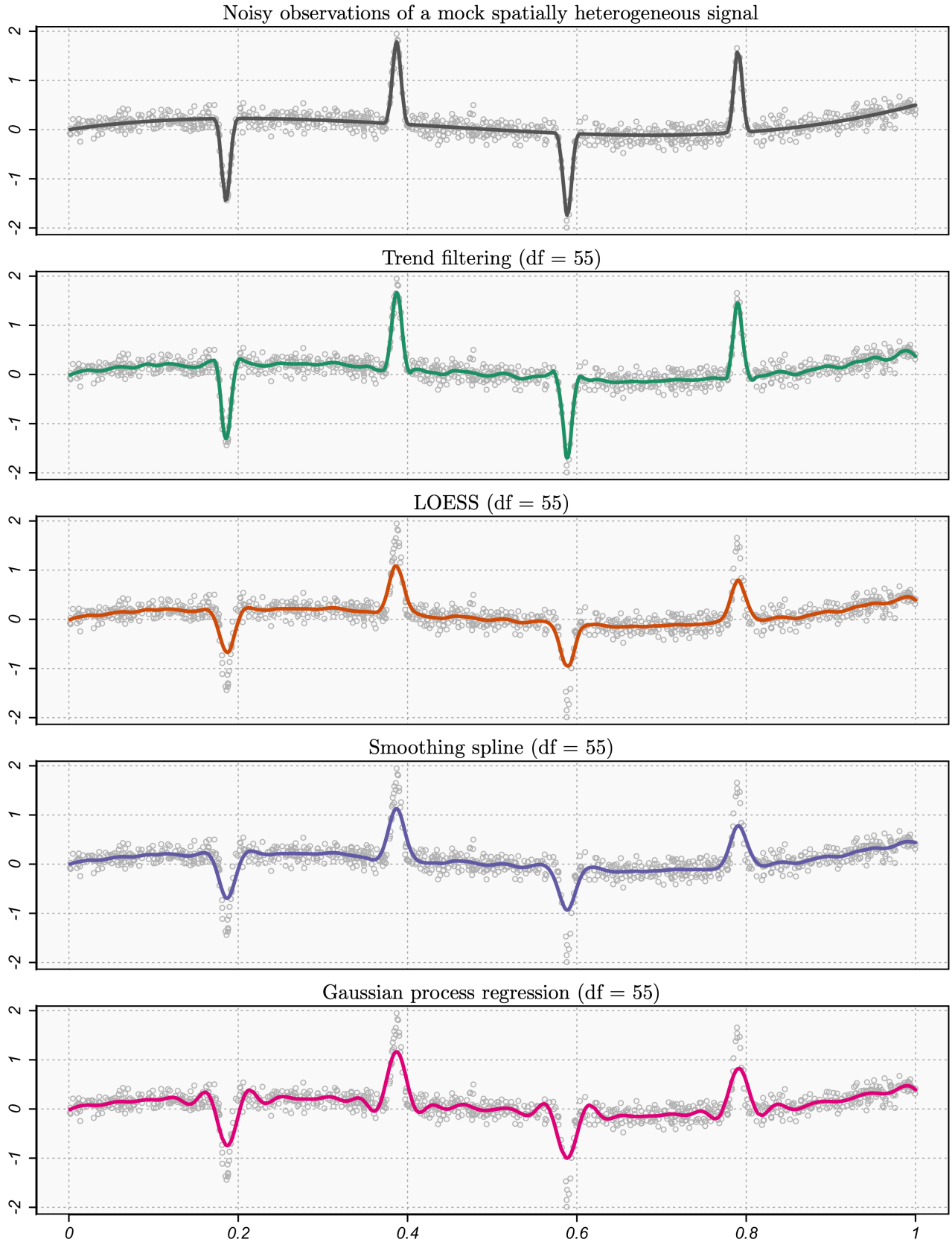

Figure 1. Comparison of statistical methods on data simulated from a spatially heterogeneous signal. Each statistical estimator is fixed to have 55 effective degrees of freedom in order to facilitate a direct comparison. The trend filtering estimator is able to sufficiently distribute its effective degrees of freedom such that it simultaneously recovers the smoothness of the global trend, as well as the abrupt localized features. The LOESS, smoothing spline, and Gaussian process regression each estimates the smooth global trend reasonably well here, but significantly oversmooths the sharp peaks and dips. Here, we utilize quadratic trend filtering (see Section 3.2).

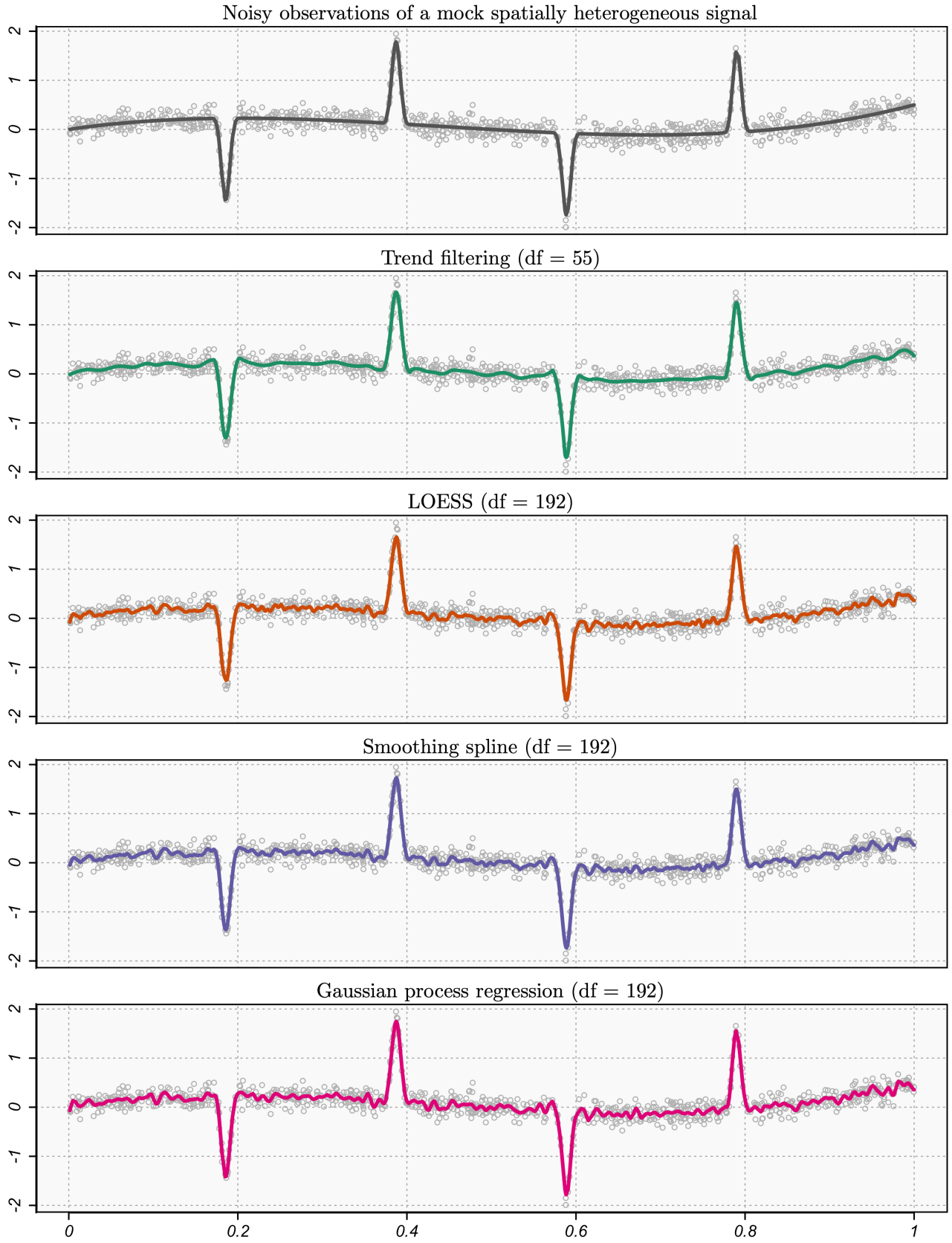

Figure 2. (Continued): Comparison of statistical methods on data simulated from a spatially heterogeneous signal. Here, each of the linear smoothers (i.e. the LOESS, smoothing spline, and Gaussian process regression) is fixed at 192 effective degrees of freedom—the complexity necessary for each estimator to recover the sharp localized features approximately as well as the trend filtering estimator with 55 effective degrees of freedom. While the linear smoothers now estimate the four abrupt features well, each severely overfits the data in the other regions of the input domain.

least-squares minimization problem:

$$\begin{aligned} \min_{\{\beta_j\}} \quad & \sum_{i=1}^{n} \left(f(t_i) - \sum_j \beta_j \eta_j(t_i) \right)^2 \\ \text{s.t.} \quad & \sum_{j \geq k+2} \mathbb{1}\{\beta_j \neq 0\} = p \\ & p \geq 0 \end{aligned} \tag{21}$$

where $p \geq 0$ is the number of knots in the spline and $\mathbb{1}(\cdot)$ is the indicator function satisfying

$$\mathbb{1}\{\beta_j \neq 0\} = \begin{cases} 1 & \beta_j \neq 0, \\ 0 & \beta_j = 0. \end{cases} \tag{22}$$

Furthermore, note that the equality constraint on the basis coefficients excludes those of the "first" $k+1$ basis functions that span the space of global polynomials and only counts the number of active basis functions that produce knots. The variable-knot regression spline optimization is therefore a problem of finding the *best subset* of knots for the regression spline estimator. Due to the sparsity of the coefficient constraint, the variable-knot regression spline estimator allows for highly locally-adaptive behavior for estimating signals that exhibit varying degrees of smoothness. However, the problem itself cannot be solved in polynomial time, requiring an exhaustive combinatorial search over all $\sim 2^n$ feasible models. It is common to utilize stepwise procedures based on iterative addition and deletion of knots in the active set, but these partial searches over the feasible set inherently provide no guarantee of finding the optimal global solution to (21).

In order to make the connection to trend filtering more explicit it is helpful to reformulate the constrained minimization (21) into the following penalized unconstrained minimization problem:

$$\min_{\{\beta_j\}} \quad \sum_{i=1}^{n} \left(f(t_i) - \sum_j \beta_j \eta_j(t_i) \right)^2 + \gamma \sum_{j \geq k+2} \mathbb{1}(\beta_j \neq 0), \tag{23}$$

where $\gamma > 0$ is a hyperparameter that determines the number of knots in the spline and the sum of indicator functions serves as a smoothness "penalty" on the ordinary least-squares minimization. Penalized regression is a popular area of statistical methodology (see, e.g., Hastie et al. 2009), in which the cost functional (i.e. the quantity to be minimized) quantifies a tradeoff between the training error of the estimator (here, the squared residuals) and the statistical complexity of the estimator (here, the number of knots in the spline). In particular, (23) is known as an ℓ_0-penalized least-squares regression because of the penalty's connection to the mathematical ℓ_0 vector quasi-norm.

3.1.2 *Smoothing splines*

Smoothing splines counteract the computational issue faced by variable-knot regression splines by simply placing knots at all of the observed inputs $t_1, \ldots, t_n$ and regularizing the smoothness of the fitted spline. For example, letting $\mathcal{G}$ be the space of all cubic natural splines with knots at $t_1, \ldots, t_n$, the cubic smoothing spline is the solution to the optimization problem

$$\min_{m \in \mathcal{G}} \quad \sum_{i=1}^{n} \big(f(t_i) - m(t_i)\big)^2 + \gamma \int_a^b \big(m''(t)\big)^2 dt, \tag{24}$$

where m'' is the second derivative of m and $\gamma > 0$ tunes the amount of regularization. Letting $\eta_1, \ldots, \eta_n$ be a basis for cubic natural splines with knots at the observed inputs, (24) can be equivalently stated as a minimization over the basis coefficients:

$$\min_{\{\beta_j\}} \quad \sum_{i=1}^{n} \left(f(t_i) - \sum_j \beta_j \eta_j(t_i) \right)^2 + \gamma \sum_{j,k=1}^{n} \beta_j \beta_k \omega_{jk} \tag{25}$$

where

$$\omega_{jk} = \int_a^b \eta_j''(t) \eta_k''(t) dt. \tag{26}$$

The cost functional (25) is differentiable and leads to a linear system with a special sparse structure (i.e. bandedness), which yields a solution that can both be found in closed-form and computed very quickly—in $O(n)$ elementary operations. This particular choice of cost functional, however, produces an estimator that is a linear combination of the observations—a *linear smoother*. Therefore, as discussed and demonstrated in Section 2, smoothing splines are suboptimal for estimating spatially heterogeneous signals. Equation (25) is known as an ℓ_2-penalized least-squares regression because of the penalty's connection to the mathematical ℓ_2 vector-norm.

3.2 Definition

Trend filtering can be viewed as a blending of the strengths of variable-knot regression splines (local adaptivity and interpretability) and the strengths of smoothing splines (simplicity and speed). Mathematically, this is achieved by choosing an appropriate set of basis functions and penalizing the least-squares problem with an ℓ_1 norm on the basis coefficients (sum of absolute values), instead of the ℓ_0 norm of variable-knot regression splines (sum of indicator functions) or the ℓ_2 norm of smoothing splines (sum of squares).

This section is primarily summarized from Tibshirani (2014) and Wang et al. (2014). Let the inputs be ordered with respect to the index, i.e. $t_1 < \cdots < t_n$. For the sake of simplicity, we consider the case when the inputs $t_1, \ldots, t_n \in (a, b)$ are equally spaced with $\Delta t = t_{i+1} - t_i$. See the aforementioned papers for the generalized definition of trend filtering to unequally spaced inputs.

For any given integer $k \geq 0$, the kth order trend filtering estimate is a piecewise polynomial of degree k with knots *automatically selected* at a sparse subset of the observed inputs $t_1, \ldots, t_n$. In Figure 3, we provide an example of a trend-filtered data set for orders $k = 0, 1, 2$, and 3. Specifically, the panels of the figure respectively display piecewise constant, piecewise linear, piecewise quadratic, and piecewise cubic fits to the data with the automatically-selected knots indicated by the tick marks on the horizontal axes. Constant trend filtering is equivalent to total variation denoising (Rudin et al. 1992), as well as special forms of the fused lasso of Tibshirani et al. (2005) and the variable fusion estimator of Land & Friedman (1996). Linear trend filtering was independently proposed by Steidl et al. (2006) and

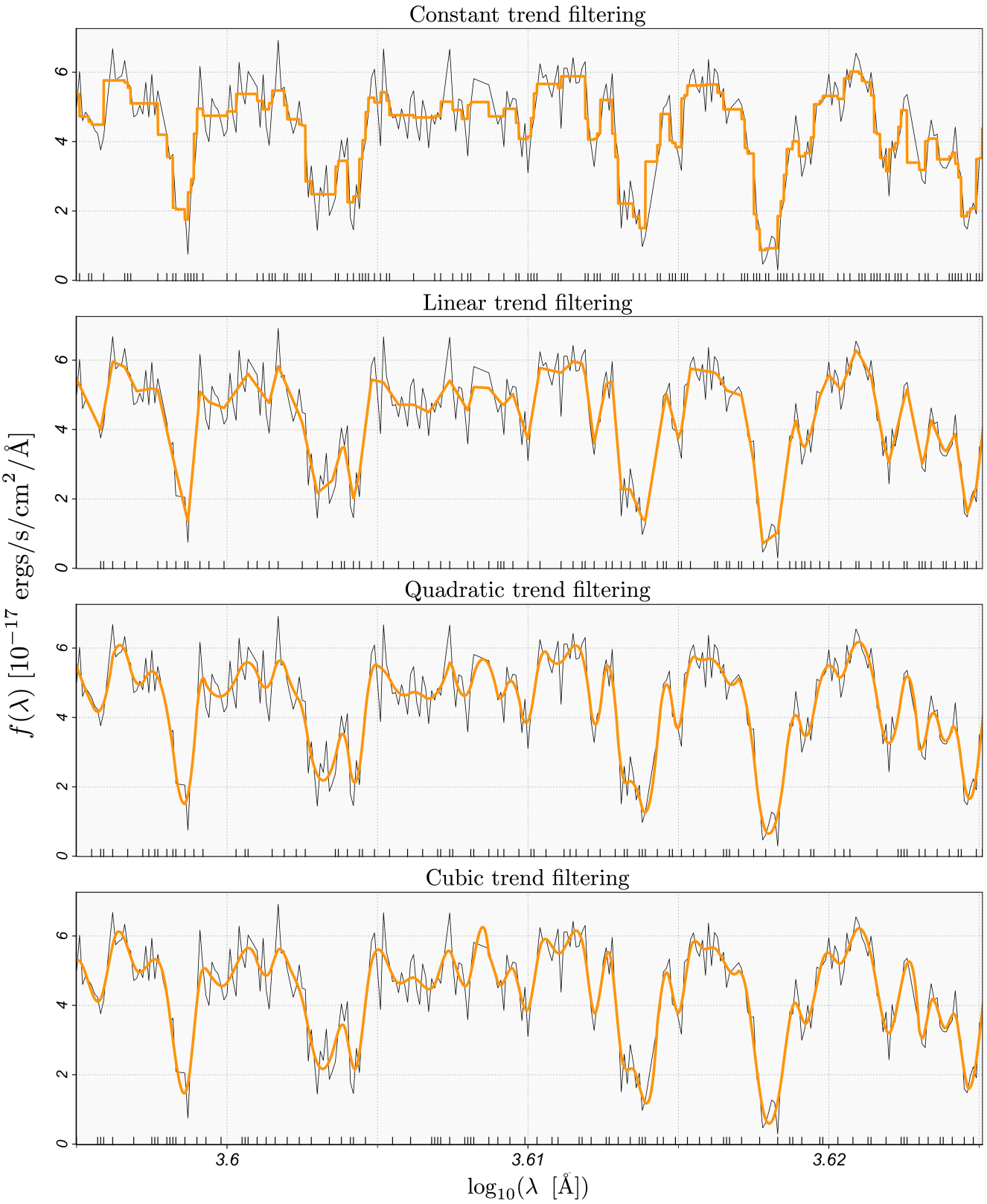

Figure 3. Piecewise polynomials with adaptively-chosen knots produced by trend filtering. From top to bottom, we show trend filtering estimates of orders $k = 0, 1, 2$ and 3, which take the form of piecewise constant, piecewise linear, piecewise quadratic, and piecewise cubic polynomials, respectively. The adaptively-chosen knots of each piecewise polynomial are indicated by the tick marks along the horizontal axes. The constant trend filtering estimate is discontinuous at the knots, but we interpolate here for visual purposes. The data set is taken from the Lyman-α forest of a mock quasar spectrum (Bautista et al. 2015), sampled in logarithmic-angstrom space. We study this phenomenon in detail in Section 4.

Kim et al. (2009). Higher-order polynomial trend filtering ($k \geq 2$) was developed by Tibshirani & Taylor (2011) and Tibshirani (2014). In the Figure 3 example, the quadratic and cubic trend filtering estimates are nearly visually indistinguishable, and this is true in general. Although, as we see here, trend filtering estimates of different orders typically select different sets of knots.

Like the spline methods discussed in Section 3.1, for any order $k \geq 0$, the trend filtering estimator has a basis representation

$$m(t) = \sum_{j=1}^{n} \beta_j h_j(t), \tag{27}$$

but, here, $\{h_1, \ldots, h_n\}$ is the *falling factorial* basis

$$h_j(t) = \begin{cases} \prod_{i=1}^{j-1}(t - t_i) & j \leq k+1, \\ \prod_{i=1}^{j-1}(t - t_{j-k-1+i}) \cdot \mathbb{1}\{t \geq t_{j-1}\} & j \geq k+2. \end{cases} \tag{28}$$

Like the truncated power basis, the first $k+1$ basis functions span the space of global kth order polynomials and the rest of the basis adds the piecewise polynomial structure. However, the knot-producing basis functions of the falling factorial basis h_j, $j \geq k+2$ have small discontinuities in their jth order derivatives at the knots for all $j = 1, \ldots, k-1$, and therefore for orders $k \geq 2$ the trend filtering estimate is *close to*, but not quite a spline. The discontinuities are small enough, however, that the trend filtering estimate defined through the falling factorial basis representation is visually indistinguishable from the analogous spline produced by the truncated power basis (see Tibshirani 2014 and Wang et al. 2014). The advantage of utilizing the falling factorial basis in this context instead of the truncated power basis (or the B-spline basis) comes in the form of significant computational speedups, as we detail below.

Analogous to the continuous smoothing spline problem (24), we let $\mathcal{H}_k$ be the space of all functions spanned by the kth order falling factorial basis, and pose the trend filtering problem as a least-squares minimization with a derivative-based penalty on the fitted function. In particular, the kth order trend filtering estimator is the solution to the problem

$$\min_{m \in \mathcal{H}_k} \quad \sum_{i=1}^{n} \big(f(t_i) - m(t_i)\big)^2 + \gamma \cdot \mathrm{TV}(m^{(k)}), \tag{29}$$

where $m^{(k)}$ is the kth derivative of m, $\mathrm{TV}(m^{(k)})$ is the *total variation* of $m^{(k)}$, and $\gamma > 0$ is the model hyperparameter that controls the smoothness of the fit. When $m^{(k)}$ is differentiable everywhere in its domain, the penalty term simplifies to

$$\mathrm{TV}(m^{(k)}) = \int_a^b |m^{(k+1)}(t)| dt. \tag{30}$$

Avoiding the technical generalized definition of total variation (see, e.g., Tibshirani 2014), we can simply think of $\mathrm{TV}(\cdot)$ as a generalized L_1 norm[4] for our piecewise polynomials that possess small discontinuities in the derivatives. Again referring back to the smoothing spline problem (24), definitions (29) and (30) reveal that trend filtering can be thought of as an L_1 analog of the (L_2-penalized) smoothing spline problem. Moreover, note that unlike smoothing splines, trend filtering can produce piecewise polynomials of all orders $k \geq 0$.

Replacing m with its basis representation, i.e. $m(t) = \sum_j \beta_j h_j(t)$, yields the equivalent finite-dimensional minimization problem[5]:

$$\min_{\{\beta_j\}} \quad \sum_{i=1}^{n} \left(f(t_i) - \sum_{j=1}^{n} \beta_j h_j(t_i) \right)^2 + \gamma \cdot k! \cdot \Delta t^k \sum_{j=k+2}^{n} |\beta_j|. \tag{31}$$

The terms $k!$ and Δt^k are constants and can therefore be ignored by absorbing them into the hyperparameter γ. Visual inspection of (31) reveals that trend filtering is also analogous to the variable-knot regression spline problem (21)—namely, by replacing the ℓ_0 norm on the basis coefficients with an ℓ_1 norm. The advantage here is that the problem is now strictly convex and can be efficiently solved by various convex optimization algorithms. Furthermore, the ℓ_1 penalty still yields a sparse solution (i.e. many $\beta_j = 0$), which provides the automatic knot-selection property. Letting $\widehat{\beta}_1, \ldots, \widehat{\beta}_n$ denote the solution to (31) for a particular choice of $\gamma > 0$, the trend filtering estimate is then given by

$$\widehat{f}_0(t; \gamma) = \sum_{j=1}^{n} \widehat{\beta}_j h_j(t), \tag{32}$$

with the automatically-selected knots corresponding to the basis functions with $\widehat{\beta}_j \neq 0$, $j \geq k+1$.

The advantage of utilizing the falling factorial basis is found by reparametrizing the problem (31) into an optimization over the fitted values $m(t_1), \ldots, m(t_n)$. The problem then reduces to

$$\min_{\{m(t_i)\}} \quad \sum_{i=1}^{n} \big(f(t_i) - m(t_i)\big)^2 + \gamma \sum_{i=1}^{n-k-1} |\Delta^{(k+1)} m(t_i)| \cdot \Delta t \tag{33}$$

where $\Delta^{(k+1)} m(t_i)$ can be viewed as a discrete approximation of the $(k+1)$st derivative of m at t_i. For $k = 0$ the discrete derivatives are

$$\Delta^{(1)} m(t_i) = \frac{m(t_{i+1}) - m(t_i)}{\Delta t}, \tag{34}$$

and then can be defined recursively for $k \geq 1$:

$$\Delta^{(k+1)} m(t_i) = \frac{\Delta^{(k)} m(t_{i+1}) - \Delta^{(k)} m(t_i)}{\Delta t}. \tag{35}$$

The penalty term in (33) can be viewed as a Riemann-like discrete approximation of the integral in (30). Because of the choice of basis, the problem has reduced to a simple generalized lasso problem (Tibshirani & Taylor 2011; Arnold & Tibshirani 2016) with an identity predictor matrix and a banded[6] penalty matrix. This special structure allows the solution to be found in nearly linear time, i.e. $O(n)$ elementary operations. In this work we utilize the specialized alternating direction method of multipliers (ADMM) algorithm of Ramdas & Tibshirani (2016). This algorithm has a linear complexity per iteration, so the overall complexity is

[4] We use the upper-case notation L_p, $p = 1, 2$ for the p-norm of a continuous function, and ℓ_p, $p = 0, 1, 2$ for the p-norm of a vector.

[5] This may be recognized as a lasso regression (Tibshirani 1996), with the features being the falling factorial basis functions.

[6] A banded matrix only contains nonzero elements in the main diagonal and zero or more diagonals on either side.

	Method	Computational Complexity	Hyperparameters to estimate
Locally-adaptive	Wavelets	$O(n)$	1
	Trend filtering	$\boldsymbol{O(n^{1.5})}$	**1**
	Variable-knot regression splines	$O(n \cdot \binom{n}{p})$	1
Non-adaptive	Uniform-knot regression splines	$O(n)$	1
	Smoothing splines	$O(n)$	1
	Kernel smoothers	$O(n^2)$	1
	LOESS	$O(n^2)$	1
	Gaussian process regression	$O(n^3)$	3+

Table 1. Comparison of computational costs associated with popular one-dimensional nonparametric regression methods. The computational complexity column states the dependence on the sample size n of the number of elementary operations necessary to obtain the fitted values of each estimator (i.e. the estimator evaluated at the observed inputs). For trend filtering, the $O(n^{1.5})$ complexity represents the worst-case complexity of the Ramdas & Tibshirani (2016) convex optimization algorithm. In most practical settings the actual complexity of this algorithm is close to $O(n)$. Variable-knot regression splines require a (nonconvex) exhaustive combinatorial search over the set of possible knots and the complexity therefore includes a binomial coefficient term $\binom{n}{p} = n!/(n!(n-p)!)$, where p is the number of knots in the spline. The remaining methods are explicitly solvable and the stated complexity represents the cost of an exact calculation. The $O(n)$ complexity of wavelets relies on restrictive sampling assumptions (e.g., equally-spaced inputs, sample size equal to a power of two). The stated computational complexity of all methods represents the cost of a single model fit and does not include the cost of hyperparameter tuning. Gaussian process regression suffers from the most additional overhead in this regard because of the (often) large number of hyperparameters used to parametrize the covariance function (e.g., shape, range, marginal variance, noise variance). Each of the non-adaptive methods (linear smoothers) can be made to be locally adaptive (e.g., by locally varying the hyperparameters of the model), but at the expense of greatly increasing the dimensionality of the hyperparameter space to be searched over.

$O(nr)$ where r is the number of iterations necessary to converge to the solution. In the worst case scenario $r \sim n^{1/2}$, so the worst-case overall complexity is $O(n^{1.5})$. The practical computational speed further illustrates the value of trend filtering to astronomy, as it is readily compatible with the large-scale analysis of one-dimensional data sets that has become increasingly ubiquitous in large sky surveys. We show a comparison in Table 1 of the computational costs associated with trend filtering and other popular one-dimensional nonparametric methods.

Given the trend filtering fitted values obtained by the optimization (33) the full continuous-time representation of the trend filtering estimate follows by inverting the parametrization back to the basis function coefficients and plugging them into the basis representation (32).

Language	Recommended implementation
R	`github.com/glmgen`
C	`github.com/glmgen`
Python	`cvxpy.org`
Matlab	`http://stanford.edu/~boyd/l1_tf`
Julia	`github.com/JuliaStats/Lasso.jl`

Table 2. Recommended implementations for trend filtering in various programming languages. See Section 3.4 for details. We provide additional code at `github.com/capolitsch/trend-filtering` for selecting the hyperparameter via minimization of Stein's unbiased risk estimate (see Section 3.5) and various bootstrap methods for uncertainty quantification (see Section 3.6). Our implementations are built on top of the `glmgen` R package of Arnold et al. (2014).

3.3 Extension to heteroskedastic weighting

Thus far we have considered the simple case where the observations are treated as equally-weighted in the cost functional (33). Recall from (18) the observational data generating process and define $\sigma_i^2 = \mathrm{Var}(\epsilon_i)$ to be the noise level—the (typically heteroskedastic) uncertainty in the measurements that arises from instrumental errors and removal of systematic effects. When estimates for σ_i^2, $i = 1, \ldots, n$ accompany the observations, as they often do, they can be used to weight the observations to yield a more efficient statistical estimator (i.e. smaller mean-squared error). The error-weighted trend filtering estimator is the solution to the following minimization problem:

$$\min_{\{m(t_i)\}} \quad \sum_{i=1}^{n} \big(f(t_i) - m(t_i)\big)^2 w_i + \gamma \sum_{i=1}^{n-k-1} |\Delta^{(k+1)} m(t_i)| \cdot \Delta t, \quad (36)$$

where the optimal choice of weights is $w_i = \sigma_i^{-2}$, $i = 1, \ldots, n$. Much of the publically available software for trend filtering allows for a heteroskedastic weighting scheme (see Section 3.4).

3.4 Software

Trend filtering software is available online across various platforms. For the ADMM implementation of Ramdas & Tibshirani (2016) that we utilize in this work, implementations are available in R and C (Arnold et al. 2014), as well as Julia (Kornblith 2014). Matlab and Python implementations are available for the primal-dual interior point method of Kim et al. (2009), but only for equally-weighted linear trend filtering (Koh et al. 2008; Diamond & Boyd 2016). We provide links to our recommended implementations in Table 2. Note that in all software implementations the trend filtering hyperparameter is called λ instead of γ, which we use here to avoid ambiguity with the notation for wavelength in our spectroscopic examples.

3.5 Choosing the hyperparameter

The choice of the piecewise polynomial order k generally has minimal effect on the performance of the trend filtering estimator in terms of mean-squared error and therefore can be treated as an *a priori* aesthetic choice based on how much smoothness is desired or believed to be present. For example, we use $k = 2$ (quadratic trend filtering) throughout Sections 4 and 5 so the fitted curves are smooth, i.e. differentiable everywhere.

Given the choice of k, the hyperparameter $\gamma > 0$ is used to tune the complexity (i.e. the wiggliness) of the trend filtering estimate by weighting the tradeoff between the complexity of the estimate and the size of the squared residuals. Obtaining an accurate estimate is therefore intrinsically tied to finding an optimal choice of γ. The selection of γ is typically done by minimizing an estimate of the mean-squared prediction error (MSPE) of the trend filtering estimator. Here, there are two different notions of error to consider, namely, *fixed-input* error and *random-input* error. As the names suggest, the distinction between which type of error to consider is made based on how the inputs are sampled. As a general rule-of-thumb, we recommend optimizing with respect to fixed-input error when the inputs are regularly-sampled and optimizing with respect to random-input error on irregularly-sampled data.

Recall the DGP stated in (18) and let it be denoted by Q so that $\mathbb{E}_Q[\cdot]$ is the mathematical expectation with respect to the randomness of the DGP. Further, let $\sigma_i^2 = \mathrm{Var}(\epsilon_i)$. The fixed-input MSPE is given by

$$R(\gamma) = \frac{1}{n}\sum_{i=1}^{n} \mathbb{E}_Q\left[\left(f(t_i) - \widehat{f}_0(t_i;\gamma)\right)^2 \,\middle|\, t_1,\ldots,t_n\right] \tag{37}$$

$$= \frac{1}{n}\sum_{i=1}^{n} \left(\mathbb{E}_Q\left[\left(f_0(t_i) - \widehat{f}_0(t_i;\gamma)\right)^2 \,\middle|\, t_1,\ldots,t_n\right] + \sigma_i^2\right) \tag{38}$$

and the random-input MSPE is given by

$$\widetilde{R}(\gamma) = \mathbb{E}_Q\left[\left(f(t) - \widehat{f}_0(t;\gamma)\right)^2\right], \tag{39}$$

where, in the latter, t is considered to be a random component of the DGP with a marginal probability density $p_t(t)$ supported on the observed input interval. In each case, the theoretically optimal choice of γ is defined as the minimizer of the respective choice of error. Empirically, we estimate the theoretically optimal choice of γ by minimizing an estimate of (37) or (39). For fixed-input error we recommend Stein's unbiased risk estimate (SURE; Stein 1981; Efron 1986) and for random-input error we recommend K-fold cross validation with $K = 10$. We elaborate on SURE here and refer the reader to Wasserman (2003) for K-fold cross validation.

The SURE formula provides an unbiased estimate of the fixed-input MSPE of a statistical estimator:

$$\widehat{R}_0(\gamma) = \frac{1}{n}\sum_{i=1}^{n}\left(f(t_i) - \widehat{f}_0(t_i;\gamma)\right)^2 + \frac{2\overline{\sigma}^2 \mathrm{df}(\widehat{f}_0)}{n}, \tag{40}$$

where $\overline{\sigma}^2 = n^{-1}\sum_{i=1}^{n}\sigma_i^2$ and $\mathrm{df}(\widehat{f}_0)$ is defined in (17). A formula for the effective degrees of freedom of the trend filtering estimator is available via the generalized lasso results of Tibshirani & Taylor (2012); namely,

$$\mathrm{df}(\widehat{f}_0) = \mathbb{E}[\text{number of knots in } \widehat{f}_0] + k + 1. \tag{41}$$

We then obtain our hyperparameter estimate $\widehat{\gamma}$ by minimizing the following plug-in estimate for (40):

$$\widehat{R}(\gamma) = \frac{1}{n}\sum_{i=1}^{n}\left(f(t_i) - \widehat{f}_0(t_i;\gamma)\right)^2 + \frac{2\widehat{\overline{\sigma}}^2 \widehat{\mathrm{df}}(\widehat{f}_0)}{n}, \tag{42}$$

where $\widehat{\mathrm{df}}$ is the estimate for the effective degrees of freedom that is obtained by replacing the expectation in (41) with the observed number of knots, and $\widehat{\overline{\sigma}}^2$ is an estimate of $\overline{\sigma}^2$. If a reliable estimate of $\overline{\sigma}^2$ is not available *a priori*, a data-driven estimate can be constructed (see, e.g., Wasserman 2006). We provide R code on the corresponding author's GitHub page[7] for implementing SURE with trend filtering. The code is built on top of the `glmgen` R package of Arnold et al. (2014), which already includes an implementation of K-fold cross validation.

Because of the existence of the degrees of freedom expression (41), trend filtering is also compatible with reduced chi-squared model assessment and comparison procedures under a Gaussian noise assumption (Pearson 1900; Cochran 1952).

3.6 Uncertainty quantification

3.6.1 Frequentist

Frequentist uncertainty quantification for trend filtering follows by studying the sampling distribution of the estimator that arises from the randomness of the observational data generating process (DGP). In particular, most of the uncertainty in the estimates is captured by studying the variability of the estimator with respect to the DGP. We advise three different bootstrap methods (Efron 1979) for estimating the variability of the trend filtering estimator, with each method corresponding to a distinct analysis setting. Here, we emphasize the terminology *variability*—as opposed to the variance of the trend filtering estimator—since, by construction, as a nonlinear function of the observed data, the trend filtering estimator has a non-Gaussian sampling distribution even when the observational noise is Gaussian. For that reason, each of our recommended bootstrap approaches is based on computing sample quantiles (instead of pairing standard errors with Gaussian quantiles).

We restate the assumed DGP here for clarity:

$$f(t_i) = f_0(t_i) + \epsilon_i, \qquad t_1,\ldots,t_n \in (a,b) \tag{43}$$

where $\mathbb{E}[\epsilon_i] = 0$. We make the further assumption that the errors $\epsilon_1,\ldots,\epsilon_n$ are independent[8]. The three distinct settings we consider are:

- **S1.** The inputs are irregularly sampled
- **S2.** The inputs are regularly sampled and the noise distribution is known
- **S3.** The inputs are regularly sampled and the noise distribution is unknown

[7] `https://github.com/capolitsch/trend-filtering`

[8] If nontrivial autocorrelation exists in the noise then a block bootstrap (Kunsch 1989) will yield a better approximation of the trend filtering variability than the bootstrap implementations we discuss.

The corresponding bootstrap methods are detailed in Algorithm 1 (nonparametric bootstrap; Efron 1979), Algorithm 2 (parametric bootstrap; Efron & Tibshirani 1986), and Algorithm 3 (wild bootstrap; Wu 1986; Liu 1988; Mammen 1993), respectively. We provide code on our GitHub page for implementing each of these methods with trend filtering.

Algorithm 1 Nonparametric bootstrap for random-input uncertainty quantification

Require: Training Data $(t_1, f(t_1)), \ldots, (t_n, f(t_n))$, hyperparameters γ and k, prediction input grid $t'_1, \ldots, t'_m$

1: **for all** b in $1 : B$ **do**

2: Define a bootstrap sample of size n by resampling the observed pairs with replacement:

$$(t_1^*, f_b^*(t_1^*)), \ldots, (t_n^*, f_b^*(t_n^*))$$

3: Let $\widehat{f}_b^*(t'_1), \ldots, \widehat{f}_b^*(t'_m)$ denote the trend filtering estimate fit on the bootstrap sample and evaluated on the prediction grid $t'_1, \ldots, t'_m$

4: **end for**

Output: The full trend filtering bootstrap ensemble

$$\{\widehat{f}_b^*(t'_i)\}_{\substack{i=1,\ldots,m \\ b=1,\ldots,B}}$$

Algorithm 2 Parametric bootstrap for fixed-input uncertainty quantification (when noise distribution $\epsilon_i \sim Q_i$ is known *a priori*)

Require: Training Data $(t_1, f(t_1)), \ldots, (t_n, f(t_n))$, hyperparameters γ and k, assumed noise distribution $\epsilon_i \sim Q_i$, prediction input grid $t'_1, \ldots, t'_m$

1: Compute the trend filtering point estimate at the observed inputs:

$$(t_1, \widehat{f}_0(t_1)), \ldots, (t_n, \widehat{f}_0(t_n))$$

2: **for all** b in $1 : B$ **do**

3: Define a bootstrap sample by sampling from the assumed noise distribution:

$$f_b^*(t_i) = \widehat{f}_0(t_i) + \epsilon_i^* \qquad \text{where } \epsilon_i^* \sim Q_i, \quad i = 1, \ldots, n$$

4: Let $f_b^*(t'_1), \ldots, f_b^*(t'_m)$ denote the trend filtering estimate fit on the bootstrap sample and evaluated on the prediction grid $t'_1, \ldots, t'_m$

5: **end for**

Output: The full trend filtering bootstrap ensemble

$$\{\widehat{f}_b^*(t'_i)\}_{\substack{i=1,\ldots,m \\ b=1,\ldots,B}}$$

Given the full trend filtering bootstrap ensemble provided by the relevant bootstrap algorithm, for any $\alpha \in (0, 1)$, a $(1 - \alpha) \cdot 100\%$ quantile-based pointwise variability band is given by

$$V_{1-\alpha}(t'_i) = \left(\widehat{f}^*_{\alpha/2}(t'_i),\ \widehat{f}^*_{1-\alpha/2}(t'_i)\right), \qquad i = 1, \ldots, m \quad (44)$$

where

$$\widehat{f}^*_\beta(t'_i) = \inf_g \left\{ g : \frac{1}{B} \sum_{b=1}^{B} \mathbb{1}\{\widehat{f}_b^*(t'_i) \le g\} \ge \beta \right\}, \qquad \beta \in (0, 1). \quad (45)$$

Algorithm 3 Wild bootstrap for fixed-input uncertainty quantification (when noise distribution is not known *a priori*)

Require: Training Data $(t_1, f(t_1)), \ldots, (t_n, f(t_n))$, hyperparameters γ and k, prediction input grid $t'_1, \ldots, t'_m$

1: Compute the trend filtering point estimate at the observed inputs:

$$(t_1, \widehat{f}_0(t_1)), \ldots, (t_n, \widehat{f}_0(t_n))$$

2: Let $\widehat{\epsilon}_i = f(t_i) - \widehat{f}_0(t_i)$, $i = 1, \ldots, n$ denote the residuals

3: **for all** i **do**

4: Define a bootstrap sample by sampling from the following distribution:

$$f_b^*(t_i) = \widehat{f}_0(t_i) + u_i^* \qquad i = 1, \ldots, n$$

where

$$u_i^* = \begin{cases} \widehat{\epsilon}_i(1 + \sqrt{5})/2 & \text{with probability } (1 + \sqrt{5})/(2\sqrt{5}) \\ \widehat{\epsilon}_i(1 - \sqrt{5})/2 & \text{with probability } (\sqrt{5} - 1)/(2\sqrt{5}) \end{cases}$$

5: Let $f_b^*(t'_1), \ldots, f_b^*(t'_m)$ denote the trend filtering estimate fit on the bootstrap sample and evaluated on the prediction grid $t'_1, \ldots, t'_m$

6: **end for**

Output: The full trend filtering bootstrap ensemble

$$\{\widehat{f}_b^*(t'_i)\}_{\substack{i=1,\ldots,m \\ b=1,\ldots,B}}$$

Analogously, bootstrap sampling distributions and variability intervals for observable parameters of the signal may be studied by deriving a bootstrap parameter estimate from each trend filtering estimate within the bootstrap ensemble. For example, in Sections 5.2 and 5.4 we examine the bootstrap sampling distributions of several observable parameters of exoplanet transits and supernovae, respectively.

3.6.2 Bayesian

There is a well-studied connection between ℓ_1-penalized least-squares regression and a Bayesian framework (see, e.g., Tibshirani 1996; Figueiredo 2003; Park & Casella 2008). A discussion specific to trend filtering can be found in Faulkner & Minin (2018).

3.7 Relaxed trend filtering

We are indebted to Ryan Tibshirani for a private conversation that motivated the discussion in this section. Trend filtering can be generalized to allow for greater flexibility through a technique that we call *relaxed trend filtering*[9]. Although the traditional trend filtering estimator is already highly flexible, there are certain settings in which the relaxed trend filtering estimator provides nontrivial improvements. In our experience, these typically correspond to settings where the optimally-tuned trend filtering estimator selects very few knots. For example, we use relaxed trend fil-

[9] We choose this term because the generalization of trend filtering to relaxed trend filtering is analogous to the generalization of the lasso (Tibshirani 1996) to the relaxed lasso (Meinshausen 2007).

tering in Section 5.2 to model the detrended, phase-folded light curve of a Kepler star with a planetary transit event.

The relaxed trend filtering estimate is defined through a two-stage sequential procedure in which the first stage amounts to computing the traditional trend filtering estimate discussed in Section 3.2. Recall the trend filtering minimization problem (31). For any given order $k \in \{0, 1, 2, \dots\}$ and hyperparameter $\gamma > 0$, let us amend our notation so that

$$\widehat{f}_0^{TF}(t) = \sum_{j=1}^{n} \widehat{\beta}_j^{TF} h_j(t) \tag{46}$$

denotes the basis representation of the traditional trend filtering estimate. Further, define the index set

$$\mathcal{K}_\gamma = \left\{ 1 \le j \le n \mid \widehat{\beta}_j^{TF} \neq 0 \right\} \tag{47}$$

that includes the indices of the non-zero falling factorial basis coefficients for the given choice of γ. Now let $\widehat{\beta}_j^{OLS}$, $j \in \mathcal{K}_\gamma$, denote the solution to the ordinary least-squares (OLS) minimization problem

$$\min_{\{\beta_j\}} \quad \sum_{i=1}^{n} \left(f(t_i) - \sum_{j \in \mathcal{K}_\gamma} \beta_j h_j(t_i) \right)^2, \tag{48}$$

and define the corresponding OLS estimate as

$$\widehat{f}_0^{OLS}(t) = \sum_{j \in \mathcal{K}_\gamma} \widehat{\beta}_j^{OLS} h_j(t). \tag{49}$$

That is, the OLS estimate (49) uses trend filtering to find the knots in the piecewise polynomial, but then uses ordinary least-squares to estimate the reduced set of basis coefficients. The relaxed trend filtering estimate is then defined as a weighted average of the traditional trend filtering estimate and the corresponding OLS estimate:

$$\widehat{f}_0^{RTF}(t) = \phi \widehat{f}_0^{TF}(t) + (1 - \phi) \widehat{f}_0^{OLS}(t), \tag{50}$$

for some choice of relaxation hyperparameter $\phi \in [0, 1]$.

In principle, it is preferable to jointly optimize the trend filtering hyperparameter γ and the relaxation hyperparameter ϕ, e.g. via cross validation. However, it often suffices to choose γ and ϕ sequentially, which in turn adds minimal computational cost on top of the traditional trend filtering procedure. Because of the trivial proximity of the falling factorial basis to the truncated power basis (established in Tibshirani 2014 and Wang et al. 2014), it is sufficient to let $\widehat{f}_0^{OLS}$ be the kth order regression spline with knots at the input locations selected by the trend filtering estimator. In heteroskedastic settings, as discussed in Section 3.3, a piecewise polynomial or regression spline fit by weighted least-squares should be used in place of the OLS estimate (49).

4 MAIN APPLICATION: QUASAR LYMAN-α FOREST

In this section, we use trend filtering to study the Lyman-α forest of quasar spectra. We choose to study this application in depth and then illustrate the breadth of trend filtering's utility through our discussions in Section 5.

The Lyman-α (Lyα) forest is the name given to the absorption features seen in quasar spectra which are caused by neutral hydrogen (H I) in the intergalactic medium between a quasar and an observer. When emitted from an accretion disk close to the central black hole, the light from the quasar has a relatively smooth spectrum—a continuum—caused by the summed black-body emission of gas with different temperatures at different disk radii (Osterbrock & Ferland 2006). Emission lines are also seen, and their intensities and line ratios supply information on the physical conditions in the line emitting gas. At least twenty broad emission lines, broadened by high velocities and temperatures can be measured in a single AGN, along with a similar number of narrow lines from colder gas (Marziani et al. 1996). The emitted spectrum therefore already consists of a superposition of components with varying degrees of smoothness. The Lyα forest arises when this spectrum is further processed with the addition of absorption lines. Light moving towards the observer is redshifted into resonance with the Lyα transition of H I, and the strength of absorption features is dictated by the densities of intergalactic material along the line of sight (Rauch 1998). The smoothness of the absorption lines varies depending on the gas pressure, and thermal doppler broadening (Gnedin & Hui 1998; Peeples et al. 2010). Sharper absorption features, metal lines, are also caused by other intergalactic species, such as C IV, O VI and Mg II (Hellsten et al. 1998; Pieri et al. 2010). The usefulness of the Lyα forest as a cosmological probe (e.g., Palanque-Delabrouille et al. 2015) stems from its relationship to the matter density field in the Universe, effectively mapping out structure along each quasar-observer line of sight (e.g., Croft et al. 1997; Lee et al. 2014). In order to extract this information from noisy spectra and separate it from other components, it is useful to have a method that can deal with the complexities outlined above, i.e. one that can naturally adapt to varying degrees of smoothness without extensive tuning.

The relative fluctuations in the Lyα forest transmitted flux fraction are of primary interest since they possess a monotonic relationship with the relative distribution of the absorbing H I. We utilize trend filtering to first denoise the spatially heterogeneous flux signal in an observed Lyα forest. Estimates for the fluctuations in transmitted flux due to absorbing H I are then typically produced by coupling the denoised Lyα forest with estimates for the quasar continuum and the cosmic mean transmitted flux in the Lyα forest. We take an alternative approach: directly estimating the mean flux level—defined as the product of the continuum and cosmic mean transmitted flux—as in Croft et al. (2002). The mean flux level is a very smooth, spatially homogeneous function within the truncated Lyα forest restframe. It is therefore appropriate to use a linear smoother (see Section 2) for this stage of estimation. Specifically, we use local polynomial regression (LOESS; Cleveland 1979; Fan & Gijbels 1996; Loader 1999). In this section, we illustrate these methods on a mock quasar Lyα forest from Bautista et al. (2015) and a real quasar Lyα forest from the Baryon Oscillation Spectroscopic Survey Data Release 12 (BOSS DR12; Alam et al. 2015) of the Sloan Digital Sky Survey III (SDSS-III; Eisenstein et al. 2011; Aihara et al. 2011).

Historically, Lyα forest analyses have typically utilized kernel smoothers (e.g., Croft et al. 2002; Kim et al. 2004), wavelets (e.g., Theuns & Zaroubi 2000), or Gaussian processes (e.g., Palanque-Delabrouille et al. 2013).

Input	Definition	Range (quasar at $z = z_0$)
λ	Observed wavelength	$\overline{\Lambda}(z_0)$
ν	Rest wavelength	$\overline{\Lambda}_{\text{rest}}(z_0) = \overline{\Lambda}(z_0)/(1+z_0)$
z	Redshift	$\Pi(z_0) = \overline{\Lambda}(z_0)/\lambda_{\text{Ly}\alpha} - 1$
ζ	Log-wavelength (scaled)	$Z(z_0) = 10^4 \cdot \log_{10}(\overline{\Lambda}(z_0))$

Table 3. Various input spaces utilized for the Lyα forest analysis. Notation of functions is held constant, e.g. $\delta_F(\cdot)$, and an alteration of the input variable implicitly indicates a change of input spaces. Logarithmic wavelengths are scaled for numerical stability of the trend filtering optimization algorithm.

4.1 Notation

Suppose we observe a quasar located at redshift $z = z_0$. Ignoring systematic effects such as sky contamination and interstellar extinction for the moment, the observational DGP of the Lyα forest can be assumed to follow the model

$$f(\lambda) = f_0(\lambda) + \epsilon(\lambda), \qquad \lambda \in \Lambda(z_0), \tag{51}$$

$$= \overline{F}(\lambda) \cdot C(\lambda) \cdot \big(1 + \delta_F(\lambda)\big) + \epsilon(\lambda), \tag{52}$$

where $f(\lambda)$ is the observed flux at wavelength λ, $f_0(\lambda)$ is the flux signal, $\epsilon(\lambda)$ is zero mean white Gaussian noise, $\Lambda(z_0) = (\lambda_{\text{Ly}\beta},\ \lambda_{\text{Ly}\alpha}) \cdot (1+z_0)$ is the redshifted Lyα forest, $C(\lambda)$ is the flux of the unabsorbed quasar continuum, $F(\lambda) = f_0(\lambda)/C(\lambda)$ is the transmitted flux fraction, $\overline{F}(\lambda) = \mathbb{E}[F(\lambda)]$ is the mean transmitted flux fraction (over the sky) in the Lyα forest at redshift $z = \lambda/\lambda_{\text{Ly}\alpha} - 1$, and

$$\delta_F(\lambda) = F(\lambda)/\overline{F}(\lambda) - 1 \tag{53}$$

is the fluctuation about the mean Lyα transmitted flux at redshift $z = \lambda/\lambda_{\text{Ly}\alpha} - 1$. Here, δ_F is the quantity we are primarily interested in estimating since $\delta_F \propto \delta_{\text{H I}}^{-1}$ at each fixed redshift, where $\delta_{\text{H I}}$ is the density of H I. The estimation of the flux signal f_0 is viewed as an ancillary step.

Although, in principle, it is preferable to study the full spectral range $\Lambda(z_0)$ we have found that, in the nonparametric setting, estimating the quasar continuum near the localized Lyα and Lyβ emission peaks at the boundaries of the Lyα forest reduces the estimation accuracy in the interior of $\Lambda(z_0)$. Therefore, in this work we limit our analysis to the truncated Lyα forest range

$$\overline{\Lambda}(z_0) = (1045\ \text{Å}\ , 1195\ \text{Å}) \cdot (1 + z_0). \tag{54}$$

We simplify notation in this work by changing the input space of the functions introduced above by merely altering the input variable. For example, with respect to δ_F, we maintain the notation $\delta_F(\cdot)$ for all inputs λ, ν, z, ζ, while it is understood that a proper change of input spaces has taken place. The various input spaces are defined in Table 3.

4.2 Trend filtering the observed flux

We use quadratic trend filtering to estimate the flux signal f_0 of the observational model (51). In both BOSS DR12 and the Bautista et al. (2015) mock catalog, the quasar spectra are sampled on equally-spaced grids in logarithmic wavelength space with $\Delta \log_{10}(\lambda_i) = 10^{-4}$ dex (in logarithmic angstroms). Furthermore, flux measurement variances are provided by the BOSS pipeline (Bolton et al. 2012), accounting for the statistical uncertainty introduced by photon noise, CCD read noise, and sky-subtraction error. We correct the BOSS spectrum for interstellar extinction with the Cardelli et al. (1989) extinction law and the Schlafly & Finkbeiner (2011) dust map.

We fit the trend filtering estimator on the equally-spaced logarithmic grid and tune the complexity by minimizing Stein's unbiased risk estimate (SURE) of the fixed-input mean-squared error (42). More precisely, we fit the trend filtering estimator in the input space $Z(z_0) = 10^4 \cdot \log_{10}(\overline{\Lambda}(z_0))$, as defined in Table 3, where we add the scaling to unit spacing for numerical stability of the trend filtering convex optimization.

4.3 Nonparametric continuum estimation

We utilize a modified Croft et al. (2002) approach to propagate the trend filtering estimate for the flux signal f_0 from Section 4.2 into an estimate for the fluctuation field δ_F along a line of sight to an observed quasar. Namely, given the trend filtering estimate $\widehat{f_0}$, we directly estimate the smooth mean flux level defined as the product $m = \overline{F} \cdot C$ and then define the δ_F estimates via the transformation $\widehat{\delta}_F := \widehat{f_0}/\widehat{m} - 1$. We carry out the estimation of m via a wide-kernel LOESS smooth of the trend filtering estimate, with the specific bandwidth of the kernel selected by optimizing over a large sample of mock spectra (detailed in Section 4.4). We find that regressing on the fitted values of the trend filtering estimate—instead of the observational DGP (51)—significantly improves the accuracy and robustness of the δ_F estimates. We carry out the LOESS estimation in the Lyα restframe $\overline{\Lambda}_{\text{rest}}(z_0)$ (see Table 3) in order to remove the effect of redshifting on the smoothness of m. The LOESS estimation of m is a fully nonparametric procedure and provides a reduction in bias over popular parametric approaches such as low-order power laws and principal components analyses (PCA). The sole assumption of our LOESS approach is that, in the restframe, the mean flux level m always has a fixed degree of smoothness, defined by an optimal fixed kernel bandwidth. There is of course a bias-variance tradeoff here; namely, the decreased bias comes with a modest increase in variance compared to a parametric power law or low-dimensional PCA model. Our decision in favor of the LOESS approach directly reflects our stance that low bias is preferable to low variance in this context since statistical uncertainty due to estimator variability is tracked by our uncertainty quantification (Section 4.5), while uncertainty due to modeling bias is not easily quantifiable. Therefore, we can be more confident that significant fluctuations in the estimated δ_F field are in fact real, and not due to statistical bias in the quasar continuum estimate.

To be explicit, the LOESS estimator for m is a regression on the data set

$$\{(\nu_i,\ \widehat{f_0}(\nu_i; \widehat{\gamma})\}_{i=1}^n, \qquad \nu_i \in \overline{\Lambda}_{\text{rest}}(z_0), \tag{55}$$

which can be viewed as arising from the DGP

$$\widehat{f_0}(\nu_i; \widehat{\gamma}) = m(\nu_i) + \rho_i, \tag{56}$$

where $\widehat{f_0}$ is the trend filtering estimate fixed at the minimum SURE hyperparameter $\widehat{\gamma}$, $e_i = \widehat{f_0}(\nu_i; \widehat{\gamma}) - f_0(\nu_i)$ are the errors of the trend filtering estimate, and $\rho_i = m(\nu_i) \cdot \delta_F(\nu_i) + e_i$ are

autocorrelated fluctuations about zero. The LOESS estimator is the natural extension of kernel regression (Nadaraya 1964; Watson 1964) to higher-order local polynomials. Given a kernel function $K(\cdot)$ with bandwidth $h > 0$, for each $i = 1, \ldots, n$, the LOESS estimator is obtained by minimizing

$$\sum_{j=1}^{n} \left(\widehat{f}_0(\nu_j; \widehat{\gamma}) - \phi_{\nu_i}(\nu_j; \beta_0, \ldots, \beta_d) \right)^2 K\left(\frac{|\nu_j - \nu_i|}{h} \right), \tag{57}$$

and letting $\widehat{m}(\nu_i) = \widehat{\beta}_0$, where $\phi_{\nu_i}(\cdot\,; \beta_0, \ldots, \beta_d)$ is a dth order polynomial centered at ν_i. Specifically, we utilize the local linear regression estimator (LLR; $d = 1$) and the Epanechnikov kernel (Epanechnikov 1967)

$$K(t) = \frac{3}{4}(1 - t^2)\mathbb{1}\{|t| < 1\}. \tag{58}$$

The LLR estimator is described in full detail by Algorithm 4. Given the trend filtering estimate $\widehat{f}_0$ and the LLR estimate $\widehat{m}$, the δ_F estimates are then defined as

$$\widehat{\delta}_F(z_i; \widehat{\gamma}) = \frac{\widehat{f}_0(z_i; \widehat{\gamma})}{\widehat{m}(z_i)} - 1, \qquad z_1, \ldots, z_n \in \Pi(z_0), \tag{59}$$

where we deliberately express $\widehat{m}$ as "hyperparameter-less" since γ has already been fixed at the minimum SURE value $\widehat{\gamma}$ and we provide the optimal LOESS bandwidth value $h_0 = 74$ Å—optimized over the large mock sample. Here, we have also done a change of variables to redshift space—our desired input domain for studying the H I density fluctuations in the IGM.

Algorithm 4 LOESS (local linear) estimator for mean flux level

Require: Training Data $\{(\nu_i, \widehat{f}_0(\nu_i; \widehat{\gamma}))\}_{i=1}^n$, Bandwidth $h_0 = 74$ Å

1: **for all** i **do**

2: Let $\widehat{\beta}_0$, $\widehat{\beta}_1$ minimize the locally weighted sum of squares

$$\sum_{j=1}^{n} \left(\widehat{f}_0(\nu_j; \widehat{\gamma}) - \beta_0 - \beta_1(\nu_j - \nu_i) \right)^2 \cdot K\left(\frac{|\nu_j - \nu_i|}{h_0} \right).$$

3: Let $\widehat{m}(\nu_i) = \widehat{\beta}_0(\nu_i)$.

4: **end for**

Output: $\{\widehat{m}(\nu_i)\}_{i=1}^n$

Although h_0 is chosen to directly optimize $\widehat{\delta}_F$ accuracy, an estimate for the quasar continuum $C(\cdot)$ arises intrinsically:

$$\widehat{C}(\nu_i) = \overline{F}(\nu_i)^{-1} \cdot \widehat{m}(\nu_i), \qquad \nu_i \in \overline{\Lambda}_{\text{rest}}(z_0), \tag{60}$$

where precise estimates of $\overline{F}$ follow from a rich literature (e.g. Bernardi et al. 2003; McDonald et al. 2005; Faucher-Giguère et al. 2008; Dall'Aglio et al. 2009; Pâris et al. 2011; Becker et al. 2013). The δ_F estimates could then be equivalently restated as

$$\widehat{\delta}_F(z_i; \widehat{\gamma}) = \frac{\widehat{F}(z_i; \widehat{\gamma})}{\overline{F}(z_i)} - 1, \qquad z_1, \ldots, z_n \in \Pi(z_0), \tag{61}$$

where

$$\widehat{F}(z_i; \widehat{\gamma}) = \widehat{f}_0(z_i; \widehat{\gamma}) / \widehat{C}(z_i). \tag{62}$$

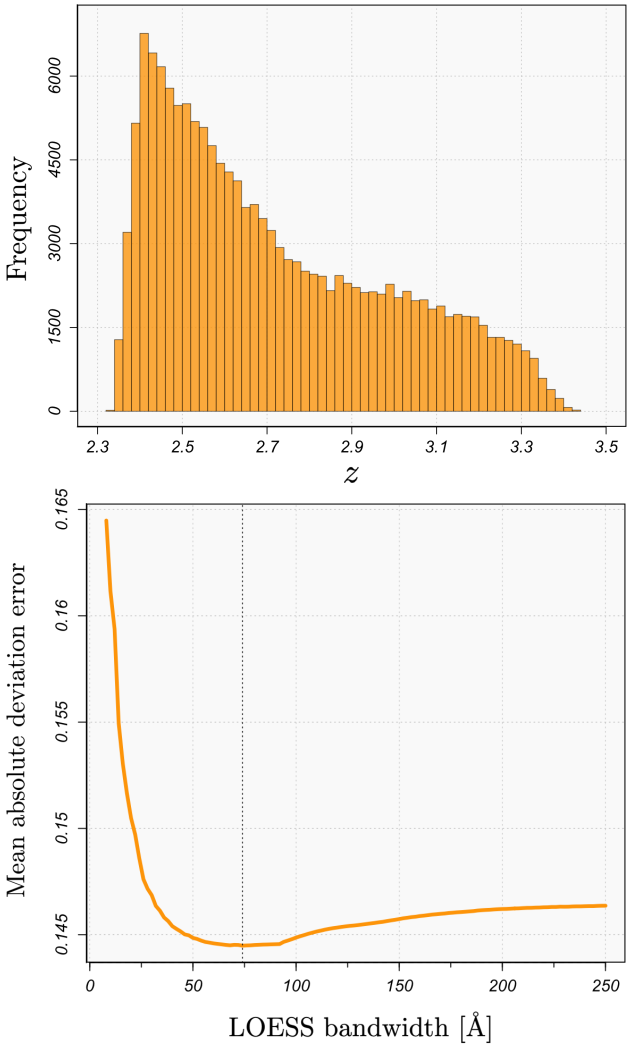

Figure 4. Top: Distribution of mock quasar redshifts (data reduction detailed in the appendix). We utilize this sample of 124,709 quasars to calibrate the optimal nonparametric continuum smoothness. **Bottom**: Mean absolute deviation error curve for selecting the optimal kernel bandwidth for the LOESS (local linear) estimator of the mean flux level, averaged over the 124,709 spectra in the mock sample. The optimal choice of bandwidth is $h_0 = 74$ Å.

4.4 Calibrating continuum smoothness

We utilize a sample of 124,709 mock quasar spectra from the Bautista et al. (2015) catalog to optimize the bandwidth of the LOESS estimator for the mean flux level that intrinsically removes the effect of the quasar continuum. Our mock data reduction is detailed in the appendix and the redshift distribution of the quasars is shown in the top panel of Figure 4.

For each mock quasar Lyα forest with DGP Q_j, $j = 1, \ldots, 124{,}709$, we first compute the trend filtering hyperparameter value that minimizes the *true* fixed-input mean-squared prediction error

$$\gamma_0^j = \underset{\gamma > 0}{\arg\min} \frac{1}{n} \sum_{i=1}^{n} \mathbb{E}_{Q_j}\left[\left(f(\zeta_i) - \widehat{f}_0(\zeta_i; \gamma) \right)^2 \,\middle|\, \zeta_1, \ldots, \zeta_n \right]. \tag{63}$$

Then, given the trend filtering restframe fitted values $\{(\nu_i,\ \widehat{f}_0(\nu_i;\gamma_0^j))\}_{i=1}^n$, we fit a LOESS estimator with bandwidth h and define the error (as a function of h) of the resulting δ_F estimator as the fixed-input mean absolute deviation (MAD) error

$$R_j(h) = \frac{1}{n}\sum_i \mathbb{E}_{Q_j}\left[\left|\delta_F(\nu_i) - \widehat{\delta}_F(\nu_i;\gamma_0^j,h)\right| \,\middle|\, \nu_1,\ldots,\nu_n\right], \tag{64}$$

where $\mathbb{E}_{Q_j}$ denotes the mathematical expectation over the randomness arising from the observational DGP Q_j. Because we can repeatedly sample from each mock quasar DGP, the expectations in (63) and (64) can be computed to an arbitrary precision. Here, we utilize 300 realizations of each DGP to approximate the mathematical expectations.

We then define the optimal choice of h as the minimizer of the summed error over the full sample of m =124,709 mock quasar spectra:

$$h_0 = \underset{h>0}{\arg\min} \sum_{j=1}^m R_j(h). \tag{65}$$

The aggregate error curve is shown in the bottom panel of Figure 4, yielding an optimal value of $h_0 = 74$ Å. We find that defining $R(h)$ as the conditional MAD error—instead of the conditional MSE—provides an essential boost in robustness that keeps the error from being dominated by a very small proportion of worst-case estimates. More complex choices of bandwidth, e.g. variable bandwidths that depend on the S/N ratio of the trend filtering estimator, the restframe pixel spacing, and/or the redshift of the quasar, do not significantly improve upon the $h_0 = 74$ Å restframe fixed bandwidth.

4.5 Uncertainty quantification

Given the assumed noise model $\epsilon_i \sim N(0,\sigma_i^2)$, $i = 1,\ldots,n$ provided by the BOSS pipeline (Bolton et al. 2012), we can construct a pointwise variability band for $\widehat{\delta}_F$ via an augmentation of the parametric bootstrap outlined in Algorithm 2. Specifically, given the parametric bootstrap ensemble of trend filtering estimates provided by Algorithm 2, we fit the mean flux level of each with the LOESS estimator detailed in Algorithm 4, and then define the $\widehat{\delta}_F$ bootstrap ensemble

$$\widehat{\delta}^*_{F,b}(z_i) = \frac{\widehat{f}^*_b(z_i)}{\widehat{m}^*_b(z_i)} - 1, \qquad i = 1,\ldots,n,\quad b = 1,\ldots,B, \tag{66}$$

where, for each $b = 1,\ldots,B$, $\widehat{m}^*_b$ is the LOESS estimate fit to the data set $\{(\nu_i, \widehat{f}^*_b(\nu_i))\}_{i=1}^n$. Note that refitting the LOESS estimator on each bootstrap realization allows us to track the extra variability introduced into the δ_F estimates by the uncertainty in the continuum estimate. Analogous to (44), a $(1-\alpha)\cdot 100\%$ quantile-based pointwise variability band for $\widehat{\delta}_F$ is then given by

$$V_{1-\alpha}(z_i) = \left(\widehat{\delta}^*_{F,\alpha/2}(z_i),\ \widehat{\delta}^*_{F,1-\alpha/2}(z_i)\right), \qquad i = 1,\ldots,n. \tag{67}$$

where

$$\widehat{\delta}^*_{F,\beta}(z_i) = \inf_g \left\{ g : \frac{1}{B}\sum_{b=1}^B \mathbb{1}\{\widehat{\delta}^*_{F,b}(z_i) \le g\} \ge \beta \right\}, \tag{68}$$

for any $\beta \in (0,1)$.

4.6 Results

A mock quasar spectrum from Bautista et al. (2015) and a real quasar spectrum from the Baryon Oscillation Spectroscopic Survey (BOSS; Alam et al. 2015) are displayed in Figure 5, with the results of our Lyα forest analysis overlaid. Starting with the top panel, the quadratic trend filtering estimate is fit on the equally-spaced observations in logarithmic wavelength space and then transformed to the restframe wavelength space, where the LOESS estimate for the mean flux level—the product of the continuum and cosmic mean Lyα absorption—is then fit to the trend filtering fitted values. The δ_F estimates are then computed according to (59) and displayed in redshift space in the second panel, where they closely track the true δ_F defined by (53). Furthermore, the 95% bootstrap variability band defined in (67) can be seen to almost fully cover the true δ_F signal. The estimated δ_F can be interpreted as an inversely proportional proxy for the deviations from the mean H I density in the intervening intergalactic medium at each redshift—with negative values of δ_F corresponding to (epoch-relative) over-densities of H I and positive values corresponding to under-densities.

The third and fourth panels are the analogous plots for a BOSS quasar spectrum Lyα forest (Data Release 12, Plate = 6487, MJD = 56362, Fiber = 647). The quasar is located in the northern galactic cap at (RA, Dec, z) $\approx$ (196.680°, 31.078°, 2.560).

5 FURTHER APPLICATIONS

The analysis of signals possessing varying degrees of smoothness permeates many areas of astronomy. In this section, we discuss a variety of further applications for which trend filtering may find use. For the sake of brevity, we discuss these applications in less detail than the Lyα forest analysis in Section 4. Naturally, we expect trend filtering may find many uses in astronomy beyond those we explicitly discuss.

The applications we discuss in this section can be grouped into two broad (and often intertwined) categories: (1) deriving estimates of observable parameters from trend-filtered observations; and (2) using trend filtering to construct spectral/light-curve templates of astronomical objects/events. In Section 5.1, we discuss constructing spectral template libraries for astronomical objects by trend filtering coadded spectroscopic observations. We illustrate our approach on quasar, galaxy, and stellar spectra from the Sloan Digital Sky Survey. Emission-line parameters can also be robustly estimated by fitting radial basis functions (e.g., Gaussians) to trend-filtered estimates near emission lines. In Section 5.2, we use relaxed trend filtering to model the detrended, phase-folded light curve of a Kepler stellar system with a transiting exoplanet. We derive estimates and full uncertainty distributions for the transit depth and total transit duration. In Section 5.3, we use trend filtering to denoise a detrended, phase-folded Kepler light curve of an eclipsing binary (EB) system. We illustrate that trend filtering provides significant improvements upon the popular `polyfit` method of Prša et al. (2008) that is used to model Kepler EB light curves and derive observable parameters. In Section 5.4, we discuss using trend filtering to construct light-curve templates of supernova (SN) explosions. We illustrate this approach on a SN light curve obtained from the

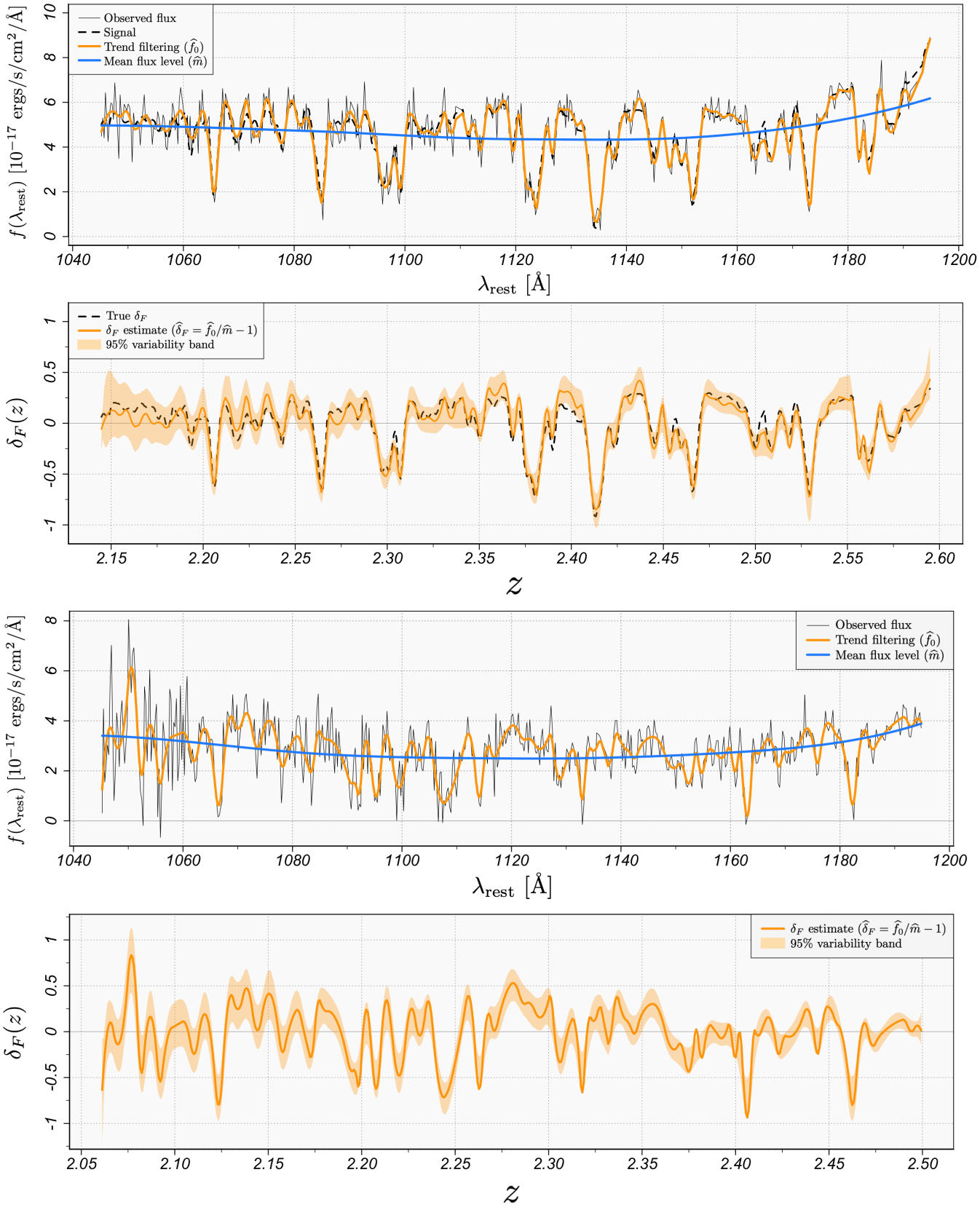

Figure 5. Results of Lyα forest analysis. **Top panel**: Lyα forest of a mock quasar spectrum (Bautista et al. 2015) in the restframe, with the quadratic trend filtering estimate shown in orange and the LOESS (local linear) estimate for the mean flux level shown in blue. **Second panel**: The redshift-space fluctuations in the Lyα transmitted flux fraction, with our estimate superposed. The fluctuations inversely trace the relative under- and over-densities of H I in the intervening intergalactic medium between Earth and the quasar. **Third and Fourth panels**: Analogous plots for a real quasar Lyα forest from the twelfth data release of the Baryon Oscillation Spectroscopic Survey (Alam et al. 2015; Plate = 6487, MJD = 56362, Fiber = 647). The quasar is located at (RA, Dec, z) ≈ (196.680°, 31.078°, 2.560).

Open Supernova Catalog (Guillochon et al. 2017). Furthermore, we derive estimates and full uncertainty distributions for a set of observable parameters—namely, the maximum apparent magnitude, the time of maximum, and the decline rate. Finally, in Section 5.5, we briefly discuss a different, non-data-analysis application of trend filtering. Specifically, we discuss the use of trend filtering as a tool for fast and flexible one-dimensional data reduction and compression. The flexibility of the trend filtering estimator, paired with its efficient speed and storage capabilities, make it a potentially powerful tool to include in large-scale (one-dimensional) astronomical data reduction and storage pipelines.

5.1 Spectral template generation and estimation of emission-line parameters

Automated spectral classification and redshift estimation pipelines require rich template libraries that span the full space of physical objects in the targeted set in order to achieve high statistical accuracy. In this section, we discuss using trend filtering to construct spectral templates from observational spectra. We describe the procedure here for generating a single spectral template from a well-sampled observed spectrum. Suppose we observe coadded flux measurements of a targeted source at wavelengths $\lambda_1, \ldots, \lambda_n \in \Lambda$ according to the data generating process

$$f(\lambda_i) = f_0(\lambda_i) + \epsilon_i, \tag{69}$$

where the observations have been corrected for systematic effects (e.g., sky subtraction, interstellar extinction, etc.) and the ϵ_i are mean-zero errors that arise from instrumental uncertainty and systematic miscalibrations. After removal of potentially problematic pixels (e.g., near bright sky lines), let $\widehat{f_0}(\lambda)$, $\lambda \in \Lambda$ denote the trend filtering estimate fit to the observations. Given a confident object classification and redshift estimate z_0 (e.g., determined by visual inspection), we then define the restframe spectral template

$$b(\lambda_{\text{rest}}) = \widehat{f_0}(\lambda/(z_0+1)), \qquad \lambda_{\text{rest}} \in \Lambda/(z_0+1), \tag{70}$$

and store it in the respective object template library.

In Figure 6, we show three optical coadded spectra from the twelfth data release of the Baryon Oscillation Spectroscopic Survey (BOSS DR12; Alam et al. 2015) of the Sloan Digital Sky Survey III (SDSS-III; Eisenstein et al. 2011; Aihara et al. 2011). The figure is zoomed to a subinterval of the optical range for visual clarity and the spectra are easily identifiable as a quasar, a galaxy, and a star, respectively. We fit an error-weighted quadratic trend filtering estimate to each spectrum in the logarithmic-angstrom wavelength space in which the BOSS spectra are gridded, and tune the hyperparameter to minimize Stein's unbiased risk estimate (see Section 3.5). The trend filtering estimates give good results, adequately adapting to even the strongest emission and absorption features in each spectrum.

As in the BOSS spectroscopic pipeline (Bolton et al. 2012), after a spectral classification and redshift measurement have been precisely determined, emission-line parameter estimates can then be obtained by fitting Gaussian radial basis functions to the emission lines of the spectrum "best fit"—nonlinearly optimizing the amplitudes, centroids, and widths. We propose that the trend filtering estimate of a spectrum be used as the "best fit" for this type of procedure, e.g. instead of the low-dimensional principal components models currently used by the BOSS pipeline. The relative magnitudes of the emission-line parameter estimates can then be used to determine object subclassifications.

5.2 Exoplanet transit modeling

In this section we discuss the use of trend filtering for modeling the photometric time series of an extrasolar planet transiting its host star. Given a phase-folded stellar light curve, corrected for stellar variability and spacecraft motion systematics, trend filtering can be used to automatically produce fully nonparametric estimates and uncertainties for the transit depth and total transit duration.

We demonstrate our approach on long-cadence photometric observations of Kepler-10 (KOI-72, KIC 11904151; Borucki et al. 2010). Kepler-10 is confirmed to host at least two exoplanets: Kepler-10b (KOI-72 b, KIC 11904151 b; Batalha et al. 2011) and Kepler-10c (KOI-72 c, KIC 11904151 c; Fressin et al. 2011). Each planet was first detected via the transit method—a measurable periodic dimming in the photometry caused by the planet crossing in front of the host star. Here, we use trend filtering to estimate a nonparametric transit model for Kepler-10c and derive depth and duration measurements. The results of our analysis are displayed in Figure 7. The top panel displays a sample of the Kepler-10 long-cadence (30-min. increment), quarter-stitched, median detrended, relative flux light curve processed by the Kepler pipeline (Jenkins et al. 2010), which we accessed from the NASA Exoplanet Archive (Akeson et al. 2013). The observed transit events of Kepler-10c are indicated by the vertical dashed lines. The middle panel displays the light curve (with 1σ error bars) after phase-folding with respect to the ~45.29 day orbital period of Kepler-10c and zooming in on the transit event. We fit a relaxed quadratic trend filtering estimate (see Section 3.7) to the phased data, weighted by the measurement variances provided by the Kepler pipeline and tuned by sequential K-fold cross validation. The optimal relaxation hyperparameter is $\widehat{\phi} = 0.14$, indicating that relaxation significantly improves the traditional trend filtering estimate in this setting. In particular, we find that relaxation allows the estimate to faithfully capture the sharp transitions corresponding to the beginning of the ingress phase and the end of the egress phase. The relaxed trend filtering estimate is overlaid on the phase-folded light curve, along with 95% variability bands. Estimates for the transit depth and total transit duration follow immediately from the relaxed trend filtering estimate, as detailed below. The estimated inception and termination of the transit event are indicated by the vertical dashed lines in the middle panel. The nonparametric bootstrap sampling distributions (see Algorithm 1) of the transit depth and total transit duration measurements are displayed in the bottom panel. Our point estimates for the transit depth and total transit duration for Kepler-10c are $\widehat{\delta} = 488.292$ ppm and $\widehat{T} = 6.927$ hours, respectively.

The knot-selection property of trend filtering is particularly appealing in this setting because it provides interpretation as to where the transit event begins and ends. Specifically, we define our estimate of the inception of the transit event $\widehat{T}_0$ as the leftmost knot selected by the trend filtering

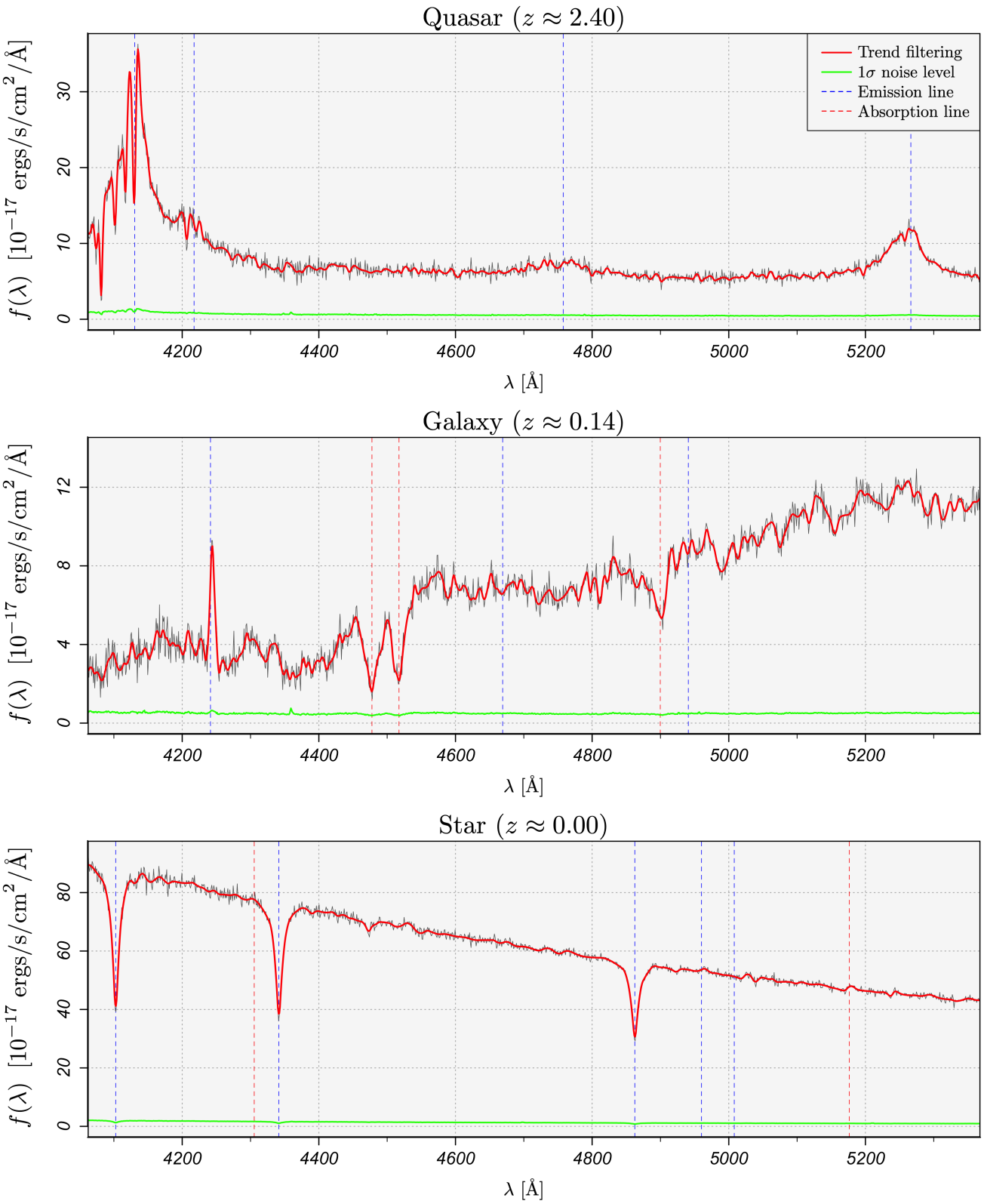

Figure 6. Optical coadded spectra collected by the Baryon Oscillation Spectroscopic Survey (Alam et al. 2015) of the Sloan Digital Sky Survey III (Eisenstein et al. 2011; Aihara et al. 2011). From top to bottom, a quasar (DR12, Plate = 7140, MJD = 56569, Fiber = 58) located at (RA, Dec, z) ≈ (349.737°, 33.414°, 2.399), a galaxy (DR12, Plate = 7140, MJD = 56569, Fiber = 68) located at (RA, Dec, z) ≈ (349.374°, 33.617°, 0.138), and a star (DR12, Plate = 4055, MJD = 55359, Fiber = 84) located at (RA, Dec, z) ≈ (236.834°, 0.680°, 0.000). We fit a quadratic trend filtering estimate to each spectrum in the logarithmic wavelength space in which the observations are equally spaced, and optimize the hyperparameter by minimizing Stein's unbiased risk estimate. Given confidently determined redshifts (e.g., determined by visual inspection), the trend filtering estimate for each object can be scaled to the restframe and stored as a spectral template. Furthermore, emission-line parameter estimates for a spectrum can be obtained by fitting Gaussian radial basis functions to the emission lines of the trend filtering estimate.

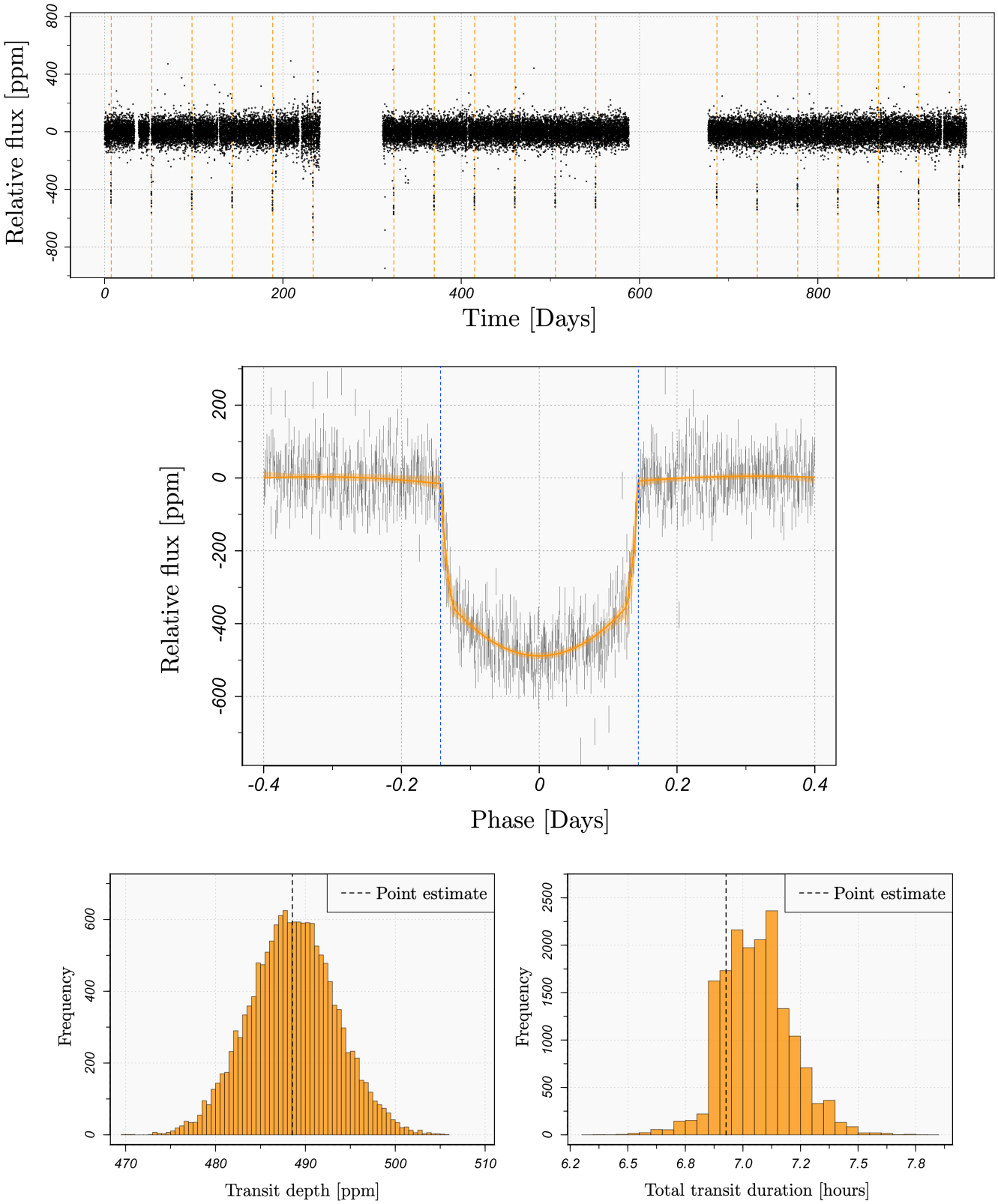

Figure 7. Kepler-10c transit light curve analysis. **Top**: Long-cadence (30-min.), quarter-stitched, median detrended, relative flux light curve (`LC_DETREND`) of the confirmed exoplanet host Kepler-10 (KOI-072, KIC 11904151; Batalha et al. 2011), processed by the Kepler pipeline (Jenkins et al. 2010) and obtained from the NASA Exoplanet Archive (Akeson et al. 2013). Vertical lines indicate the observed transit events of the system's second confirmed planet Kepler-10c (KOI-072 c, KIC 11904151 c; Fressin et al. 2011). **Middle**: Phase-folded transit light curve for Kepler-10c (~45.29 day orbital period) with 1σ error bars. The error-weighted relaxed trend filtering estimate, optimized by sequential K-fold cross validation, is superposed with 95% variability bands. The estimated inception and termination of the transit event are indicated by the vertical dashed lines. The estimated transit depth and total transit duration are $\widehat{\delta}$ = 488.292 ppm and $\widehat{T}$ = 6.927 hours, respectively. **Bottom**: Bootstrap sampling distributions of the transit depth and transit duration estimates.

estimator and we define our estimate of the termination of the transit event $\widehat{T}_1$ as the rightmost knot[10]. The total transit duration estimate then follows as $\widehat{T} = \widehat{T}_1 - \widehat{T}_0$. Naturally, we define our transit depth estimate $\widehat{\delta}$ to be the minimum of the relaxed trend filtering estimate.

It is thus far unclear to us whether trend filtering can also reliably detect the end of the ingress and beginning of the egress phases—e.g. via knot selection or examining changes in the estimated derivates—and therefore also provide nonparametric ingress/egress duration measurements. We recommend pairing trend filtering with the traditional analytical transit model search (e.g., Mandel & Agol 2002) for these particular measurements. That is, given the transit depth and total transit duration measurements provided by trend filtering, an analytical planet model can be fit over a parameter space that is constrained by the trend filtering parameter measurements. Coupling the two methods in this way therefore also provides significant computational speedups over a traditional single-stage analytical model search since it greatly reduces the dimensionality of the parameter space to be searched over. Furthermore, the relaxed trend filtering estimate may provide a benchmark χ^2 statistic for the constrained analytical model comparison.

A dedicated paper on this application of trend filtering is forthcoming.

5.3 Eclipsing binary modeling

In this section we discuss how trend filtering can further improve the work of the Kepler Eclipsing Binary working group, specifically in regard to the Eclipsing Binaries via Artificial Intelligence (EBAI) pipeline used to characterize Kepler eclipsing binary stars via their phase-folded light curves (Prša et al. 2008, 2011; Slawson et al. 2011; Slawson, Prša, Welsh, Orosz, Rucker, Batalha, Doyle, Engle, Conroy, Coughlin & et al. Mat). The EBAI pipeline utilizes an artificial neural network (ANN) to estimate a set of physical parameters for each binary pair (the temperature ratio, sum of fractional radii, photometric mass ratio, radial and tangential components of the eccentricity, fillout factor, and inclination) from the observables of the phase-folded light curve (e.g., the eclipse widths, depths, and separations). Prša et al. (2008) outline the EBAI light curve pre-processing algorithm, which they call `polyfit`, that provides the crucial step of taking a noisy, irregularly-spaced, phase-folded light curve (detrended for spacecraft motion and normalized by the median flux) and outputting a denoised and gridded phase-folded light curve, which is then fed to the ANN. We propose that trend filtering be used for this pre-processing step instead of the `polyfit` algorithm for the reasons detailed below.

An eclipsing binary (EB) light curve is characterized by periodic dips in the observed brightness that correspond to eclipse events along the line of sight to an observer. In particular, there are two eclipses per orbital period—a primary and a secondary eclipse. The primary eclipse occurs when the hotter star is eclipsed by the cooler star and produces a comparatively deep dip in observed brightness. Analogously, the secondary eclipse occurs when the cooler star is eclipsed by the hotter star and produces a comparatively shallow dip in the observed brightness. Depending on the effective temperature ratio and orbital period of the EB, the dips may range from very narrow and abrupt to very wide and smooth. In Figure 8, we display a detrended, median-normalized, long-cadence (30 min. increment) light curve of a Kepler EB (KIC 6048106; Borucki et al. 2010; Prša et al. 2011), with the primary eclipses and secondary eclipses designated by dashed red and blue lines, respectively. The orbital period of KIC 6048106 is ~1.559 days.

After phase-folding with respect to the estimated EB orbital period and centering the primary eclipse at `Phase = 0`, the purpose of the EBAI light-curve pre-processing step is to faithfully extract the signal of the phase-folded light curve and evaluate it on a regular grid so that it can then be input into the EBAI ANN. We show a comparison of the `polyfit` algorithm of Prša et al. (2008) and our trend filtering approach in Figure 9 on the phase-folded KIC 6048106 light curve. We choose a relatively high S/N light curve here in order to elucidate the significant statistical bias that underlies `polyfit`. The `polyfit` algorithm fits a piecewise quadratic polynomial by weighted least-squares with four knots selected by a randomized computational search over the phase space. The piecewise quadratic polynomial is forced to be continuous, but no smoothness constraints are placed on the derivatives of the estimate at the knots. Recalling our discussion in Section 2.1, this overly-stringent modeling assumption leads to significant statistical bias in the light-curve estimate. The bias is particularly apparent by examining the residuals of the `polyfit` estimate, which we display below the light curve. Moreover, recalling our discussion of variable-knot regression splines in Section 3.1.1, the randomized partial search over the space of feasible knots inherently provides no guarantee of finding a global solution—leaving the algorithm susceptible to extreme failure scenarios. We display a quadratic trend filtering estimate of the KIC 6048106 phase-folded light curve in the bottom panel of Figure 9, with the hyperparameter chosen by K-fold cross validation. The trend filtering estimate accurately recovers the signal of the light curve (clearly apparent here by examining a high S/N light curve) and produces a desirable random residual scatter about zero. Since the statistical bias introduced by the `polyfit` pre-processing stage propagates through to the EBAI ANN as systematic bias in the input data, we are confident that the use of trend filtering will in turn improve the error rate of the EBAI ANN output-parameter estimates.

5.4 Supernova light-curve template generation and estimation of observable parameters

In this section we demonstrate the use of trend filtering for generating light-curve templates of supernova (SN) events and estimating observable parameters. We illustrate our approach on SN 2016coi (ASASSN-16fp; Holoien et al. 2016) by constructing a B-band light-curve template from the well-sampled observations of Brown et al. (2014) and Prentice et al. (2018) and deriving nonparametric estimates and full uncertainty distributions for the maximum apparent brightness, the time of maximum, and the decline rate parameter $\Delta m_{15}(B)$ introduced by Phillips (1993). The improve-

[10] Note that the boundary points of the input space are not considered knots.

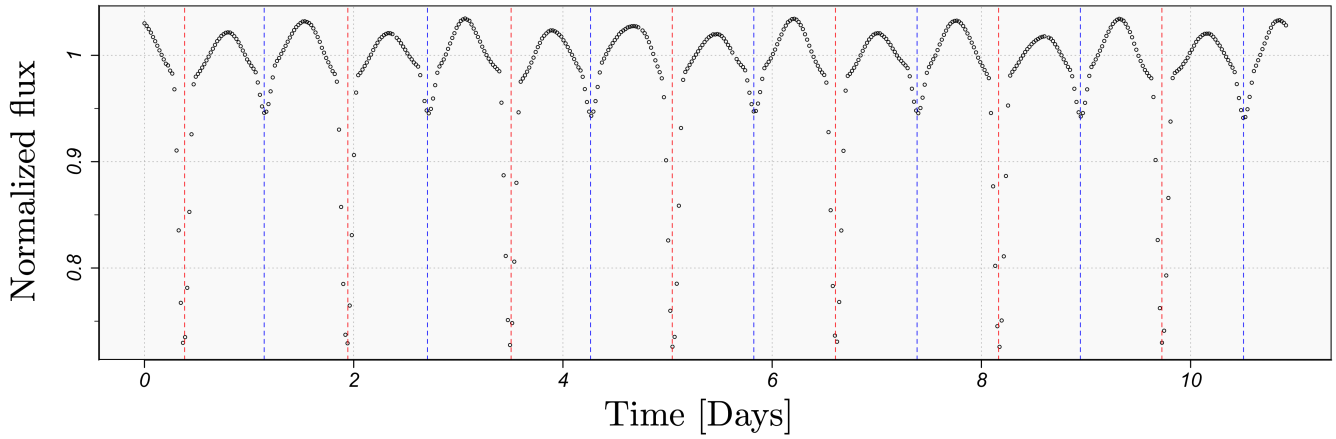

Figure 8. Long-cadence (30-min. increment), detrended, median-normalized light curve of a Kepler eclipsing binary system (KIC 6048106; Borucki et al. 2010; Prša et al. 2011). The vertical red lines mark the primary eclipses (the eclipses of the hotter star) and the vertical blue lines mark the secondary eclipses (the eclipses of the cooler star). KIC 6048106 has an orbital period of ~1.559 days.

ment yielded by trend filtering as a tool for SN light-curve template generation, compared to, for example, the `SNooPy` cubic smoothing spline approach of the Carnegie Supernova Project (CSP; Contreras et al. 2010; Burns et al. 2010; Burns et al. 2014) primarily corresponds to light curves with an especially bright peak magnitude and fast decline rate. In such cases, trend filtering is better able to recover the abruptness of the peak, the initial sharp decline, and the subsequent slow decay. This behavior is particularly characteristic of Type Ia SNe (e.g., Woosley et al. 2007). In cases where the peak is not particularly prominent, trend filtering and cubic smoothing splines produce nearly identical estimates. Our procedure for generating the SN light-curve templates requires reasonably well-sampled observations (in particular, with the initial observation occurring before maximum light). The resulting template libraries can then be used to classify SNe with partially-sampled light curves and derive parameter estimates (e.g., Belokurov et al. 2004).

The SN light-curve template generation procedure is analogous to the spectral template generation procedure discussed in Section 5.1, so we discuss it in less formal detail here. Naturally, the same procedure can also be implemented for generating fixed-time spectral templates of SN events. Given a well-sampled light curve, corrected for systematic effects (e.g., K-corrections and interstellar reddening), we propose the use of quadratic trend filtering to generate a "best fit" to the observations. Given a confident type classification, the trend filtering estimate can then be stored as a light-curve template in the respective library.

We show a B-band light curve for SN 2016coi (ASASSN-16fp; Holoien et al. 2016) in the top panel of Figure 10. The light curve is an aggregation of observations collected by Brown et al. (2014) and Prentice et al. (2018), which we accessed from the Open Supernova Catalog (Guillochon et al. 2017). SN 2016coi was discovered on May 27, 2016 (UT 2016-05-27.55) by the All Sky Automated Survey for SuperNovae (ASAS-SN; Shappee et al. 2014) in the galaxy UGC 11868 at redshift $z \approx 0.0036$. The classification of SN 2016coi currently remains intermediate between Type Ib and Type Ic (Elias-Rosa et al. 2016; Kumar et al. 2018; Prentice et al. 2018; Terreran et al. 2019). We fit a quadratic trend filtering estimate to the observations, weighted by measurement uncertainties and with the hyperparameter selected by K-fold cross validation. The trend filtering estimate, along with 95% nonparametric bootstrap variability bands, is overlaid in the top panel of the figure. In the bottom panels we show the univariate nonparametric bootstrap sampling distributions for the estimates of the maximum apparent magnitude, the time of maximum, and the decline rate—defined as the relative change in the B-magnitude light curve from maximum light to the magnitude 15 days after the maximum (Phillips 1993). We also show a bivariate bootstrap sampling distribution for maximum apparent magnitude versus decline rate. The bimodality in the bootstrap sampling distributions arises from systematic discrepancies between the two separate sets of B-band observations that form the light curve (Brown et al. 2014; Prentice et al. 2018).

5.5 Data reduction and compression

Although the primary focus of this paper is the use of trend filtering as a tool for astronomical data analysis, it also possesses potential utility for large-scale reduction and compression of one-dimensional data sets. This owes to several factors: its speed, flexibility, and representation as a sum of basis functions with a sparse coefficient vector.

Given a one-dimensional set of n observations $(t_1, f(t_1)), \ldots, (t_n, f(t_n)) \in (a, b) \times \mathbb{R}$, trend filtering can quickly provide a flexible, lower-dimensional approximation of the data where the dimensionality is controlled by the choice of the hyperparameter γ. In this context γ is a subjective choice that specifies the amount of (lossy) compression desired—unrelated to the discussion in Section 3.5. For any given choice of γ, let p be the number of knots selected by the trend filtering estimator. The corresponding continuous-time representation of this lower-dimensional approximation is fully encoded by the bounds of the observed input interval (a, b) and the sparse basis vector with $p + k + 1$ nonzero entries, which can be stored efficiently. The falling factorial basis then serves as the "dictionary" from which the continuous-time representation can be losslessly recovered. Gridded uncertainty measurements for the reduced obser-

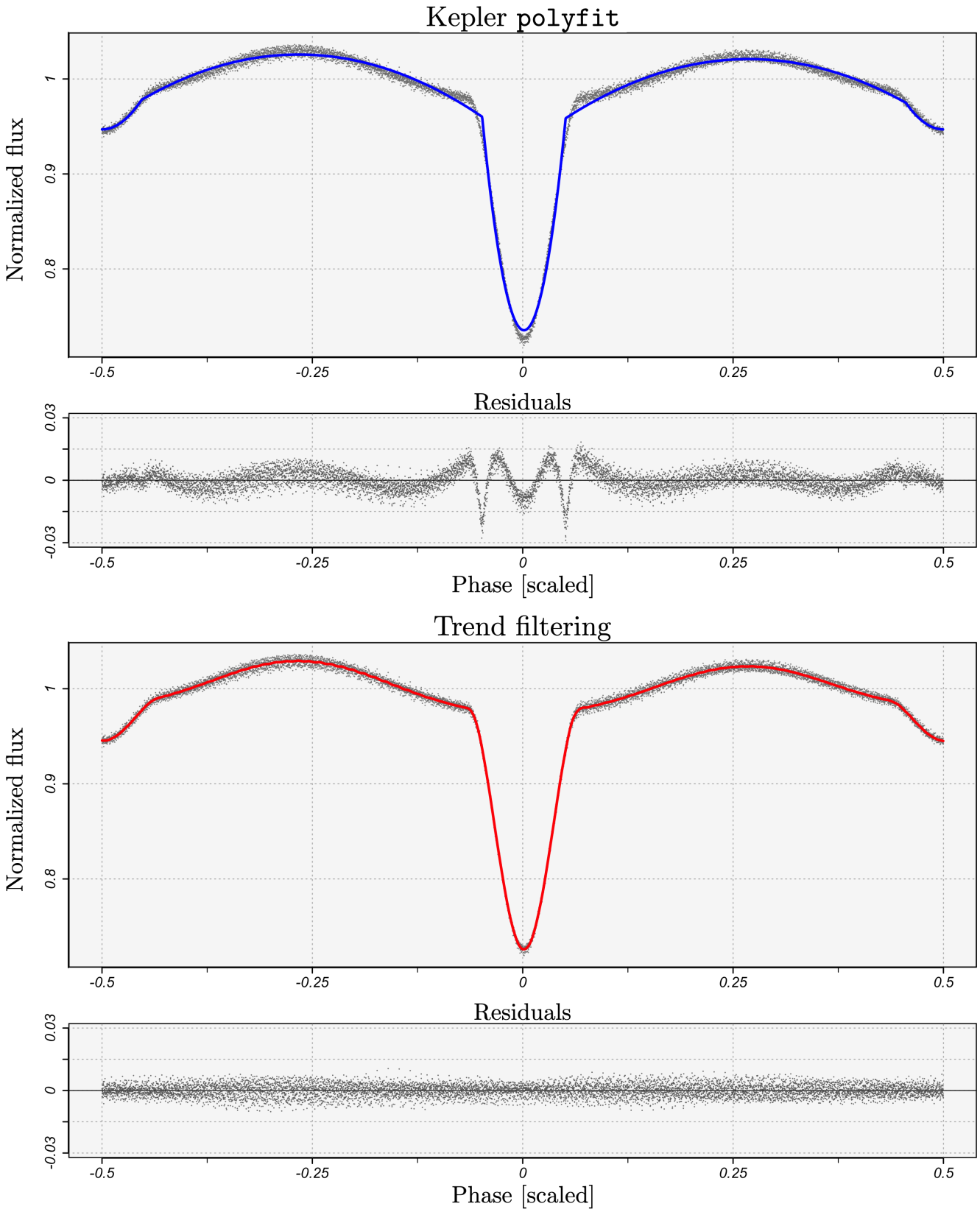

Figure 9. Comparison of the `polyfit` algorithm of Prša et al. (2008) and our trend filtering approach for denoising phase-folded eclipsing binary light curves. The light curve shown in this example comes from the Kepler eclipsing binary system KIC 6048106 (Borucki et al. 2010; Prša et al. 2011). **Top**: The `polyfit` algorithm fits a piecewise quadratic polynomial by weighted least-squares with four knots selected by a randomized search over the phase space. The estimate is constrained to be continuous but no constraints are enforced on the derivatives at the knots. The overly-stringent assumed model leads to significant statistical bias, which is readily apparent by examining the autocorrelation in the residuals. **Bottom**: Trend filtering is sufficiently flexible to accurately denoise the diverse set of signals observed in phase-folded eclipsing binary light curves. Here, the goodness-of-fit is clear by the random, mean-zero residual scatter.

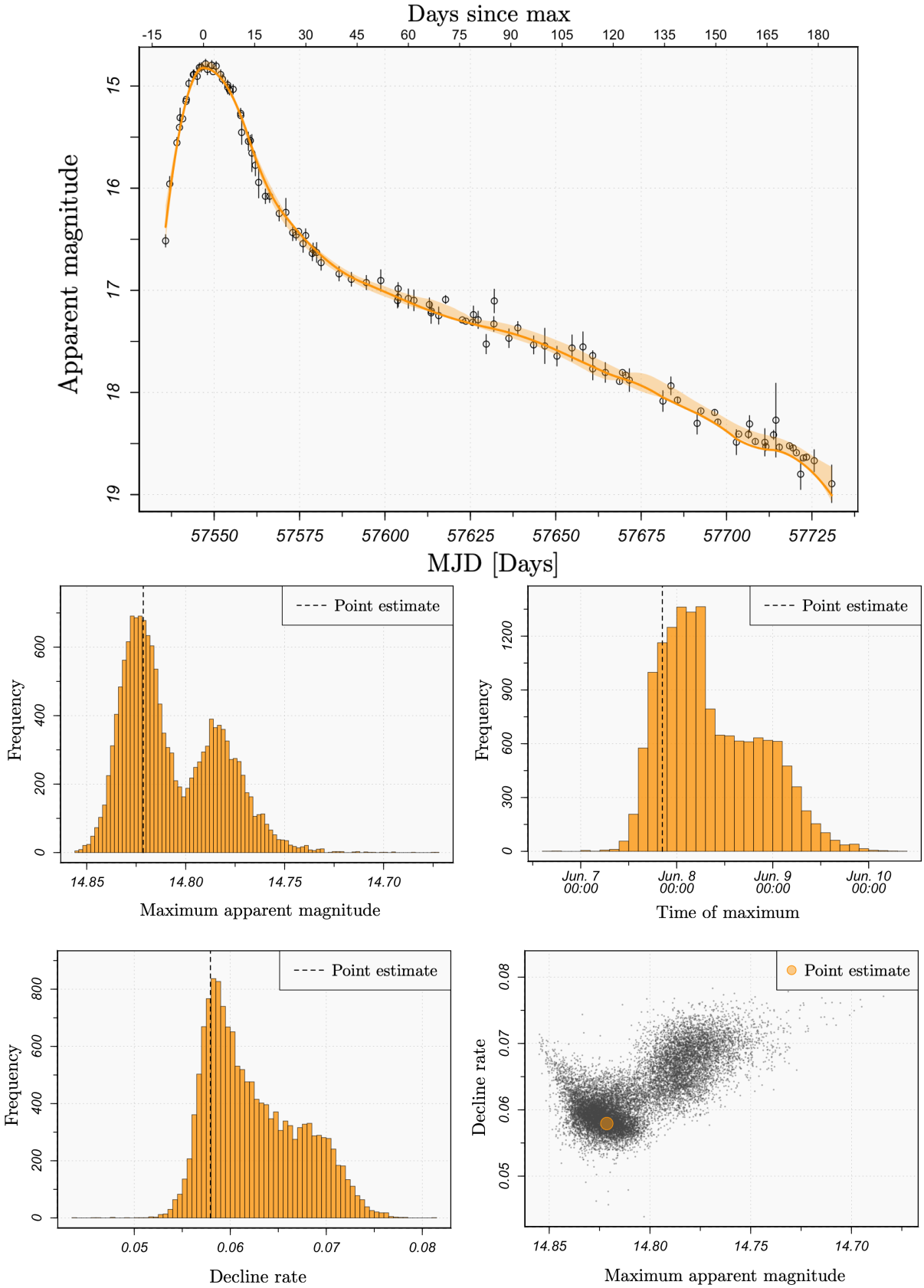

Figure 10. SN light-curve analysis (SN 2016coi). **Top**: B-band photometry of the supernova SN 2016coi (ASASSN-16 fp; Holoien et al. 2016) discovered on May 27, 2016 by the All Sky Automated Survey for SuperNovae (ASAS-SN; Shappee et al. 2014) in the galaxy UGC 11868 at redshift $z \approx 0.0036$. We fit a quadratic trend filtering estimate, tuned by K-fold cross validation, and overlay 95% nonparametric bootstrap variability bands. **Bottom**: Univariate/bivariate nonparametric bootstrap sampling distributions of the observable parameter estimates derived from the trend filtering light-curve estimate. The bimodality in the bootstrap parameter distributions arises from systematic discrepancies between the observations of the two separate observers (Brown et al. 2014; Prentice et al. 2018).

vations can also be computed and stored, though not in a sparse format, via the methods discussed in Section 3.6.

6 CONCLUDING REMARKS

The analysis of one-dimensional data arising from signals possessing varying degrees of smoothness is central to a wide variety of problems in time-domain astronomy and astronomical spectroscopy. Trend filtering is a modern statistical tool that provides a unique combination of (1) statistical optimality for estimating spatially heterogeneous signals; (2) natural flexibility for handling general sampling designs, heteroskedastic noise distributions, etc.; (3) practical computational speed, i.e. nearly linear computational complexity in the sample size; and (4) a single model hyperparameter that can be chosen via automatic data-driven methods.

In order to illustrate the broad utility of trend filtering to astronomy, we demonstrated its promising performance on a wide variety of problems across time-domain astronomy and astronomical spectroscopy. We studied the Lyman-α forest of quasar spectra with the most depth—using trend filtering to map the relative distribution of neutral hydrogen in the high redshift intergalactic medium along quasar-observer lines of sight. Furthermore, we discussed how trend filtering can be used to (1) generate galaxy, quasar, and stellar spectral templates and estimate emission-line parameters; (2) produce nonparametric models for exoplanet transit events in phase-folded stellar light curves, providing estimates for the transit depth and total duration; (3) improve upon the `polyfit` algorithm utilized by the Kepler Eclipsing Binary via Artificial Intelligence (EBAI) pipeline for denoising phase-folded eclipsing binary light curves (as a preliminary step to estimating the physical parameters); (4) generate supernova light-curve templates and produce nonparametric estimates of the maximum apparent magnitude, the time of maximum, and the decline rate; (5) quickly and efficiently compress large collections of one-dimensional data sets. Naturally, we expect trend filtering will find uses in astronomy beyond those that we explicitly discussed.

Software for trend filtering is freely available online across various platforms and we provide links to our recommendations in Table 3.4. Additionally, we make supplementary R code available on the corresponding author's GitHub page[11] for: (1) selecting the trend filtering hyperparameter by minimizing Stein's unbiased risk estimate (see Section 3.5); and (2) various bootstrap methods for trend filtering uncertainty quantification (see Section 3.6).

ACKNOWLEDGEMENTS

We gratefully thank Ryan Tibshirani for his inspiration and generous feedback on this topic. This work was partially supported by NASA ATP grant NNX17AK56G, NASA ATP grant 80NSSC18K1015, and NSF grant AST1615940.

This research contains data collected by the Sloan Digital Sky Survey III (SDSS-III). Funding for SDSS-III has been provided by the Alfred P. Sloan Foundation, the Participating Institutions, the National Science Foundation, and the U.S. Department of Energy Office of Science. The SDSS-III web site is `http://www.sdss3.org/`. SDSS-III is managed by the Astrophysical Research Consortium for the Participating Institutions of the SDSS-III Collaboration including the University of Arizona, the Brazilian Participation Group, Brookhaven National Laboratory, Carnegie Mellon University, University of Florida, the French Participation Group, the German Participation Group, Harvard University, the Instituto de Astrofisica de Canarias, the Michigan State/Notre Dame/JINA Participation Group, Johns Hopkins University, Lawrence Berkeley National Laboratory, Max Planck Institute for Astrophysics, Max Planck Institute for Extraterrestrial Physics, New Mexico State University, New York University, Ohio State University, Pennsylvania State University, University of Portsmouth, Princeton University, the Spanish Participation Group, University of Tokyo, University of Utah, Vanderbilt University, University of Virginia, University of Washington, and Yale University. This research has made use of the NASA Exoplanet Archive, which is operated by the California Institute of Technology, under contract with the National Aeronautics and Space Administration under the Exoplanet Exploration Program. This paper includes data collected by the Kepler mission. Funding for the Kepler mission is provided by the NASA Science Mission Directorate. This research contains data that was accessed from the Open Supernova Catalog, a centralized, open repository for supernova metadata, light curves, and spectra. The Open Supernova Catalog web site is `https://sne.space`. The original sources of the supernova light curve studied in this paper are credited in the text.

[11] `https://github.com/capolitsch/trend-filtering`

REFERENCES

Aigrain S., Parviainen H., Pope B. J. S., 2016, MNRAS, 459, 2408
Aihara H., et al., 2011, ApJS, 193, 29
Akeson R. L., et al., 2013, PASP, 125, 989
Alam S., et al., 2015, ApJS, 219
Arnold T. B., Tibshirani R. J., 2016, Journal of Computational and Graphical Statistics, 25, 1
Arnold T. B., Sadhanala V., Tibshirani R. J., 2014, Fast algorithms for generalized lasso problems, `https://github.com/glmgen`
Batalha N. M., et al., 2011, ApJ, 729, 27
Bautista J. E., et al., 2015, JCAP, 1505
Becker G. D., Hewett P. C., Worseck G., Prochaska J. X., 2013, MNRAS, 430, 2067
Belokurov V., Evans N. W., Le Du Y., 2004, MNRAS, 352, 233
Bernardi M., et al., 2003, AJ, 125, 32
Bolton A. S., et al., 2012, AJ, 144, 144
Borucki W. J., et al., 2010, Science, 327, 977
Brown P. J., Breeveld A. A., Holland S., Kuin P., Pritchard T., 2014, Ap&SS, 354, 89
Burns C. R., et al., 2010, AJ, 141, 19
Burns C. R., et al., 2014, ApJ, 789, 32
Cardelli J., Clayton G., Mathis J., 1989, ApJ, 345, 245
Cleveland W. S., 1979, Journal of the American Statistical Association, 74, 829
Cochran W. G., 1952, The Annals of Mathematical Statistics, 23, 315
Contreras C., et al., 2010, AJ, 139, 519
Croft R. A. C., Weinberg D. H., Katz N., Hernquist L., 1997, ApJ, 488, 532
Croft R. A. C., et al., 2002, ApJ, 581
Dall'Aglio A., Wisotzki L., Worseck G., 2009

De Boor C., 1974, in Conference on the numerical solution of differential equations. pp 12–20
De Boor C., 1978, in Applied Mathematical Sciences.
Dhawan S., Leibundgut B., Spyromilio J., Maguire K., 2015, MNRAS, 448, 1345
Diamond S., Boyd S., 2016, Journal of Machine Learning Research, 17, 1
Dimatteo I., Genovese C. R., Kass R. E., 2001, Biometrika, 88, 1055
Dimitriadis G., et al., 2017, MNRAS, 468, 3798
Donoho D. L., Johnstone I. M., 1994, Probability Theory and Related Fields, 99, 277
Donoho D. L., Johnstone I. M., 1998, The Annals of Statistics, 26, 879
Efron B., 1979, The Annals of Statistics, 7, 1
Efron B., 1986, Journal of the American Statistical Association, 81, 461
Efron B., Tibshirani R., 1986, Statistical Science, 1, 54
Eisenstein D. J., et al., 2011, AJ, 142, 72
Elias-Rosa N., et al., 2016, The Astronomer's Telegram
Epanechnikov V., 1967, Theory of Probability & its Applications, 14, 153
Fan J., 1993, The Annals of Statistics, 21, 196
Fan J., Gijbels I., 1992, The Annals of Statistics, 20, 2008
Fan J., Gijbels I., 1995, Journal of the Royal Statistical Society. Series B (Methodological), 57, 371
Fan J., Gijbels I., 1996, Local Polynomial Modeling and Its Applications. Chapman and Hall
Fan J., Gasser T., Gijbels I., Brockmann M., Engel J., 1997, Annals of the Institute of Statistical Mathematics, 49, 79
Faucher-Giguère C.-A., Lidz A., Hernquist L., Zaldarriaga M., 2008, ApJ, 688, 85
Faulkner J. R., Minin V. N., 2018, Bayesian Analysis, 13, 225
Figueiredo M. A. T., 2003, IEEE Transactions on Pattern Analysis and Machine Intelligence, 25, 1150
Fligge M., Solanki S. K., 1997, A&AS, 124, 579
Fressin F., et al., 2011, ApJS, 197, 5
Gibson N. P., Aigrain S., Roberts S., Evans T. M., Osborne M., Pont F., 2012, MNRAS, 419, 2683
Gijbels I., Mammen E., 1998, Scandinavian Journal of Statistics, 25, 503
Gnedin N. Y., Hui L., 1998, MNRAS, 296, 44
Golkhou V. Z., Butler N. R., 2014, ApJ, 787, 90
Gómez-Valent A., Amendola L., 2018, JCAP, 2018, 051
Guillochon J., Parrent J., Kelley L. Z., Margutti R., 2017, ApJ, 835, 64
Györfi L., Kohler M., Krzyzak A., Walk H., 2002, in Springer Series in Statistics.
Hall P. B., et al., 2002, ApJS, 141
Hastie T., Tibshirani R., Friedman J., 2009, The Elements of Statistical Learning: Data Mining, Inference and Prediction, 2 edn. Springer
Hellsten U., Hernquist L., Katz N., Weinberg D. H., 1998, ApJ, 499, 172
Holoien T. W.-S., et al., 2016, The Astronomer's Telegram, 9086
Howell D. A., et al., 2005, ApJ, 634, 1190
Ibragimov I. A., Hasminiskii R. Z., 1980, Zapiski Nauchnykh Seminarov LOMI (in Russian), 97, 88
Jenkins J. M., et al., 2010, ApJ, 713, L87
Jupp D. L., 1978, SIAM Journal on Numerical Analysis, 15, 328
Kim T.-S., Viel M., Haehnelt M. G., Carswell R. F., Cristiani S., 2004, MNRAS, 347, 355
Kim S.-J., et al., 2009, SIAM Review, 51, 339
Koh K., Kim S.-J., Boyd S., 2008, `l1_tf`: Software for l1 Trend Filtering, `http://stanford.edu/~boyd/l1_tf/`
Kornblith S., 2014, Lasso/Elastic Net linear and generalized linear models, `https://github.com/JuliaStats/Lasso.jl`
Kovács G., Bakos G., Noyes R. W., 2005, MNRAS, 356, 557
Kumar B., Singh A., Srivastav S., Sahu D. K., Anupama G. C., 2018, MNRAS, 473, 3776
Kunsch H. R., 1989, The Annals of Statistics, 17, 1217
Land S., Friedman J., 1996, Technical report, Variable fusion: a new method of adaptive signal regression. Department of Statistics, Stanford University
Lee K.-G., et al., 2014, ApJL, 795, L12
Lepski O. V., Mammen E., Spokoiny V. G., 1997, The Annals of Statistics, 25, 929
Liu R., 1988, The Annals of Statistics, 16, 1696
Loader C., 1999, Local Regression and Likelihood. Springer-Verlag
Mammen E., 1993, The Annals of Statistics, 21, 255
Mandel K., Agol E., 2002, ApJ, 580, L171
Maron J. L., Howes G. G., 2003, ApJ, 595, 564
Marziani P., Sulentic J. W., Dultzin-Hacyan D., Calvani M., Moles M., 1996, ApJS, 104, 37
143
McDonald P., et al., 2005, ApJ, 635, 761
Meinshausen N., 2007, Computational Statistics & Data Analysis, 52, 374
Muller H.-G., Stadtmuller U., 1987, The Annals of Statistics, 15, 610
Nadaraya E. A., 1964, Theory of Probability & its Applications, 9, 141
Nemirovskii A., 1985, Izv. Akad. Nauk. SSSR Tekhn. Kibernet. (in Russian), 3, 50
Nemirovskii A., Polyak B., Tsybakov A., 1985, Problems of Information Transmission, 21
Nussbaum M., 1985, The Annals of Statistics, 13, 984
Osterbrock D. E., Ferland G. J., 2006, Astrophysics of gaseous nebulae and active galactic nuclei
Paciorek C. J., Schervish M. J., 2004, in Advances in neural information processing systems. pp 273–280
Paciorek C. J., Schervish M. J., 2006, Environmetrics, 17, 483
Palanque-Delabrouille N., et al., 2013, A&A, 559, A85
Palanque-Delabrouille N., et al., 2015, JCAP, 2015, 011
Pâris I., et al., 2011, A&A, 530
Park T., Casella G., 2008, Journal of the American Statistical Association, 103, 681
Pearson K., 1900, The London, Edinburgh, and Dublin Philosophical Magazine and Journal of Science, 50, 157
Peeples M. S., Weinberg D. H., Davé R., Fardal M. A., Katz N., 2010, MNRAS, 404, 1281
Peiris H. V., Verde L., 2010, Phys. Rev., D81, 021302
Persson S. E., Madore B. F., Krzemiński W., Freedman W. L., Roth M., Murphy D. C., 2004, AJ, 128, 2239
Phillips M. M., 1993, ApJL, 413, L105
Pieri M. M., Frank S., Weinberg D. H., Mathur S., York D. G., 2010, ApJL, 724, L69
Prentice S. J., et al., 2018, MNRAS, 478, 4162
Prša A., Guinan E. F., Devinney E. J., DeGeorge M., Bradstreet D. H., Giammarco J. M., Alcock C. R., Engle S. G., 2008, ApJ, 687, 542
Prša A., et al., 2011, AJ, 141, 83
Ramdas A., Tibshirani R. J., 2016, Journal of Computational and Graphical Statistics, 25, 839
Rauch M., 1998, ARA&A, 36, 267
Rudin L. I., Osher S., Faterni E., 1992, Physica D: Nonlinear Phenomena, 60, 259
Schlafly E., Finkbeiner D., 2011, ApJ, 737, 103
Schmidt A. M., O'Hagan A., 2003, Journal of the Royal Statistical Society. Series B (Statistical Methodology), 65, 743
Shappee B. J., et al., 2014, ApJ, 788, 48
Slawson R. W., et al., 2011, AJ, 142, 160
Steidl G., Didas S., Neumann J., 2006, International Journal of Computer Vision, 70, 241
Stein C. M., 1981, The Annals of Statistics, 9, 1135

Stone C. J., 1982, The Annals of Statistics, 10, 1040
Tennyson J., 2019, Astronomical Spectroscopy: an Introduction to the Atomic and Molecular Physics of Astronomical Spectroscopy
Terreran G., et al., 2019, ApJ, 883, 147
Theuns T., Zaroubi S., 2000, MNRAS, 317, 989
Tibshirani R., 1996, Journal of the Royal Statistical Society. Series B (Methodological), 58, 267
Tibshirani R. J., 2014, The Annals of Statistics, 42, 285
Tibshirani R. J., 2015, Statistica Sinica, pp 1265–1296
Tibshirani R. J., Taylor J., 2011, The Annals of Statistics, 39, 1335
Tibshirani R. J., Taylor J., 2012, The Annals of Statistics, 40, 1198
Tibshirani R., Saunders M., Rosset S., Zhu J., Knight K., 2005, Journal of the Royal Statistical Society: Series B, 67, 91
Tolstov A., Nomoto K., Sorokina E., Blinnikov S., Tominaga N., Taniguchi Y., 2019, ApJ, 881, 35
Tsybakov A. B., 2008, Introduction to Nonparametric Estimation, 1st edn. Springer Publishing Company, Incorporated
Van der Vaart A. W., 1998, Asymptotic Statistics. Cambridge Series in Statistical and Probabilistic Mathematics, Cambridge University Press
Wahba G., 1990, Spline Models for Observational Data. CBMS-NSF Regional Conference Series in Applied Mathematics, Society for Industrial and Applied Mathematics
Wang Y.-X., Smola A., Tibshirani R., 2014, in Xing E. P., Jebara T., eds, Proceedings of Machine Learning Research Vol. 32, Proceedings of the 31st International Conference on Machine Learning. PMLR, Bejing, China, pp 730–738
Wang Y.-X., et al., 2016, Journal of Machine Learning Research, 17, 1
Wasserman L., 2003, All of Statistics: A Concise Course in Statistical Inference. Springer Publishing Company, Incorporated
Wasserman L., 2006, All of Nonparametric Statistics. Springer Texts in Statistics
Watson G. S., 1964, Sankhyā: The Indian Journal of Statistics, Series A, 26, 359
Woosley S. E., Kasen D., Blinnikov S., Sorokina E., 2007, ApJ, 662, 487
Wu C., 1986, The Annals of Statistics, 14, 1261

This paper has been typeset from a TEX/LATEX file prepared by the author.

APPENDIX

Mock quasar Lyman-α forest reduction

The Bautista et al. [2015] mock quasar catalog is designed to mimic the observational data generating processes of the quasar spectra released in Data Release 11 of the Baryon Oscillation Spectroscopic Survey (Alam et al. 2015). We pool the first three realizations of the mock catalog, i.e. `M3_0_3/000`, `M3_0_3/001`, and `M3_0_3/002` and remove all damped Lyα systems (DLAs), Lyman-limit systems (LLS), and broad absorption line quasars (BALs). We assume no metal absorption in the Lyα forest and correct estimation and subtraction of the sky. We mask all pixels with `and_mask` $\neq$ `0` or `or_mask` $\neq$ `0`. Finally, we retain only the spectra with $\geq$ 500 pixels in the truncated Lyα forest and those with a fixed-input-optimal trend filtering hyperparameter satisfying $\gamma_0 < 5.25$. Spectra with $\gamma_0 \geq 5.25$ correspond to the very lowest S/N observations, where the trend filtering estimate typically reduces to a global power law fit (zero knots). The final mock sample contains 124,709 quasar spectra.